Synchronization between two Hele-Shaw cells.

Angela Bernardini
Departamento de Física y Matemática Aplicada
Universidad de Navarra

January, 2004

Acknowledgments

In writing this investigation, I owe a great debt to the joint contribution of several people to whom I wish to express my deep gratitude.

First, I wish to thank the European project director Dr. Hector Mancini to make possible my presence at the department of Physics and Applied Mathematics. As he says, "Ho comprato a scatola chiusa".

I am very grateful to my scientific advisor Dr. Jean Bragard, with whom I have worked closely for many months, who has prepared and driven me for the realization of this research. But first of all, to be a friend.

I express my friendly thanks to Dr. Sergio Ardanza who contributed to the process of writing the English version and made many valuable suggestions for improving the comprehensibility and the formulation of many chapters.

Dr. Stefano Boccaletti contributed with many useful comments and precious discussions.

Many thanks are also addressed to all the department, the secretary, all my colleagues and all the professors who contributed to the completion of thesis in various way.

I thank Cecilia Wolluschek that have been my Spanish's teacher, my colleagues of journey, of party and of all the best I remember of Spain.

I thank Sara, Maria and Sergia to be my Spanish family.

I also thank my parents for their unwavering support and encouragement.

In addition, I would like to thank the University of Navarra to make possible my PhD and the European project COSYC OF SENS (Grant Number BFM 2002-02011) for the financial support.

Contents

Introduction

Thermal Convection

The origin of the term *convection* [1], from the Latin "convectio", gives an idea of "carrying with". It seems to have been applied for the first time to denote the transport of heat through fluid motion. Thermal convection arises when a thermal inhomogeneity exists in a fluid. This thermal inhomogeneity is a source of motion through different possible mechanisms, but stabilizing effects tend to dampen these motions. Generally, competition between these two opposite effects leads to an instability. The fundamental characteristic of such instabilities is the existence of a threshold beyond which there is organization of motion into a relatively ordered pattern.

H. Bénard [2] was the first person to study quantitatively the phenomenon of convection in which instability is primarily due to temperature dependence of the surface-tension. In fact, it was at the turn of the last century that Bénard reported on carefully controlled experiments of convective motions in thin horizontal liquid layers, where the lower surface was a metallic plate heated by steam and maintained at a uniform temperature, while the upper surface was in free contact with air. Bénard observed a first phase in which the fluid formed cells of almost regular shapes, nearly polygons of four to seven sides, which evolved to equal and regularly spaced hexagons.

There is a different mechanism responsible for convection in which we are more interested in this thesis i.e. the Rayleigh-Bénard convection [1], which has become an experimental and theoretical paradigm for the study of systems out of the equilibrium. The Rayleigh-Bénard experiment consists of a thin layer of fluid confined between two horizontal, spatially-uniform, constant-temperature metal plates such that the bottom plate is maintained at a constant temperature higher than the upper plate. The temperature difference generates a vertical gradient in the layer. The resulting stratification is formed by one denser layer located above another less dense. This situation is clearly unstable.

A fluid element located in the less dense region is not subjected to any upwards force, since its horizontal surroundings are of the same density. But, if we consider a small ascending displacement of the fluid element, this will be surrounded by denser regions producing an buoyancy force that will sustain the initial displacement, to which the thermal diffusivity and the viscous force will oppose. There is a threshold, due to the mechanism mentioned above, after which the dissipative effects can

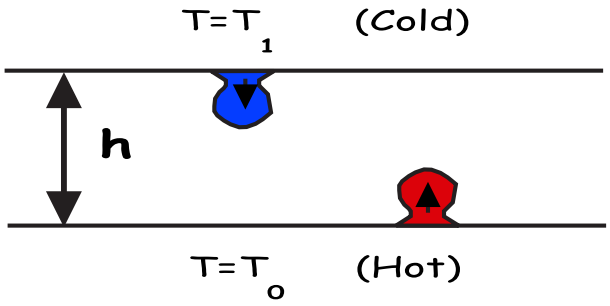

Figure 1: The geometry and physics of Rayleigh-Bénard convection. Hot goes up...cold goes down $T_0 > T_1$.

not stop the fluid motion, and convection begins. As consequence, a "dynamical" structure takes place: there is an organization of ascending and descending motions, in rolls turning clockwise or counter-clockwise successively in space.
The stability question is the following: during the time required for the fluid element to move a distance h, has the thermal diffusivity relaxed the temperature difference between the fluid element and its new surroundings?
This problem was studied theoretically by Lord Rayleigh [3] at the beginning of the twentieth century. Starting from the conservation equations he calculated the linear stability of the conductive state.

$$\begin{aligned} \frac{\partial \rho}{\partial t} &= -\nabla \cdot (\rho \mathbf{v}) \\ \frac{dT}{dt} &= \kappa \nabla^2 T \\ \rho \frac{d\mathbf{v}}{dt} &= \nu \nabla^2 \mathbf{v} - \nabla p + \rho \mathbf{g} \end{aligned} \tag{1}$$

He ignored the non linear terms and assumed that the physical properties were temperature independent, except for the density. This is the Boussinesq approximation in fluid mechanics.
This study permitted to define the so-called Rayleigh number, Ra, that is the dimensionless parameter which determines the stability of a fluid layer subjected to a destabilizing vertical thermal gradient

$$Ra = \frac{g\alpha \Delta T h^3}{\nu \kappa} \tag{2}$$

where ν is the fluid kinematic viscosity, κ is the heat diffusivity, ΔT is the temperature difference across the layer of height h, g is the acceleration of gravity and α is the thermal expansion coefficient. If Ra is higher than a certain value, motion inside of the layer will begin. Since experiments can only take place in finite containers, a number of researchers have discussed the influence of the lateral walls on the convective process in a rectangular box. A linear study of pure gravity-driven instability in rectangular containers with rigid horizontal and lateral walls was presented by Davis [4; 5]. He predicted the appearance at the threshold of "finite" rolls (cells with

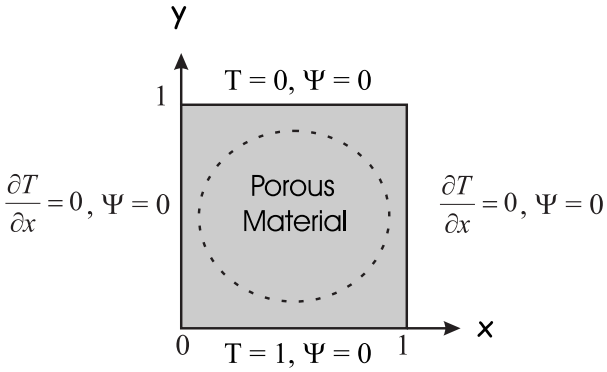

Figure 2: Convection in a porous media.

non-zero velocity components dependent on all three spatial variables) with axes parallel to the shorter side.
The results on the onset of convection in rectangular vessels have been extended to boxes of axisymmetric shape. Experiments in vessels of circular shape and large extent have been performed by Koschmieder [6; 7] also by Koster and Müller [8] and also more recently in smaller square boxes by Ondarcuhu *et al.* [9] and Ramón *et al.* [10].

Hele-Shaw and porous media

The Hele-Shaw cell was invented by British engineer Henry S. Hele Shaw before the turn of the twentieth century, and consists of two transparent plates separated by a small gap [11], so that one dimension is much smaller than the other two. It is very useful because it reduces the complicated three dimensional flow of fluid to a two dimensional flow. If the gap between the plates is sufficiently small the fluid flow between the plates held vertically and heated from below, is a good analog of the porous flow along ridge axes. For this reason, the governing equations for gap-averaged velocity components are identical with those for two-dimensional flow in a porous medium (the interested reader can see the detailed derivation in [12; 13]).

As the Rayleigh number increases above a critical value of $Ra_c = 4\pi^2$, the heat transfer process changes from conduction to convection. This first transition has already received considerable attention by Horton and Rogers (1945) [14] and Lapwood (1948) [15]. Their studies indicated that steady-state flow patterns evolved from an initially motionless system and remained unchanged for all subsequent times. It was noticed later, that under certain conditions the flow became oscillatory. The appearance of time dependent motion in a fluid layer uniformly heated from below has been suggested from Caltagirone *et al.* [16], and then Horne and O'Sullivan [17] who verified the existence of both stationary and oscillatory motions. There are more recent numerical works confirming the old results, where porous-media convection for higher Rayleigh numbers has been treated with particular attention as an illustration to the route to chaos. Cherkaoui and Wilcock [18] determined

a sequence of transitions in an open-top square porous layer heated from below: stationary - periodic - chaotic - periodic - chaotic. The flow pattern starts with a uni-cellular mode evolves to a bi-cellular and quadri-cellular mode, this last mode being the more stable convective mode. This dynamical states succession depends on the way in which the lower boundary is heated [19]. For example, if it is heated slowly enough, the temperature difference across the boundary layer is such that the effective Rayleigh number does not reach its critical value until the layer has extended well across the system, in which case only a uni-cellular mode forms. The same result occurs if a uni-cellular perturbation is applied to a uniformly stratified conduction solution. Once this lower order flow regime has become dominant then higher and more favorable flow patterns are suppressed.

Synchronization

The origin of the term *synchronization* comes from the Greek and it means "occurring in the common time" [20]. The original meaning of synchronization has been maintained up to now in the colloquial use of the word, as the capacity of objects of different nature to acquire a common regime. Synchronization phenomena are abundant in science, nature, engineering and social life. Systems as diverse as clocks, singing crickets, cardiac pacemakers, firing neurons and applauding audiences exhibit a tendency to operate in synchrony. In the year 1665 the Dutch scientist Christiaan Huygens was the first who observed and clearly described synchronization. He wrote in a letter to his father about two pendulum clocks hanging on a wall. He observed while he was sick and obliged to stay in bed for a couple of days that their oscillations coincided perfectly and the pendulum moved always in opposite directions. He correctly understood that the conformity of the rhythms of the clocks had been caused by an imperceptible motion of the beam. In his dissertation *Horologium oscillatorium* [21] he explained that the oscillations of the pendulum communicate some motion to the clocks, this motion impressed to the beam has the effect of making the pendulum come to a state of exactly contrary swings. In this way Huygens had given an exact description of *mutual synchronization* (the beam is not rigid but can vibrate slightly; the vibration is caused by the motions of both pendulum as a result the two clocks "feel" the presence of each other) due to a *coupling* (the interaction is due to the beam).

Also in the case treated in this thesis, two Hele-Shaw cells are coupled with each other and the coupling factor induces an adjustment of the rhythms leading to a mutual synchronization. In this case we have a *bidirectional coupling*.
A very different situation is the one described by a *unidirectional coupling*. Here one system evolves freely and drives the evolution of the other, so the response system is slaved to follow the dynamics of the driver system which acts as an external forcing. Furthermore the Huygens's clocks, moving in opposite directions, are an example of synchronization in *anti-phase*. Indeed, the phases of the oscillators help us to distinguish between two different synchronization regimes, see Fig. 3.
Recently, *synchronization of chaos* [22; 23] has aroused much interest in view of its

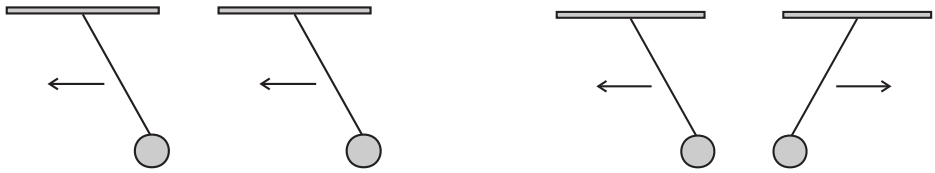

Figure 3: Possible synchronous regimes of two nearly identical oscillators. They may be synchronized in-phase, or in anti-phase.

potential applications. In particular, the use of chaotic synchronization in communication systems has been investigated by several authors [24; 25]. A dynamical system is called chaotic when its evolution is sensitive to small perturbations in its initial conditions [26]. This means that two close but different points in the phase space will have trajectories that eventually separate exponentially. In other words, the evolution of a chaotic system cannot be predicted over a long time period.

The representation of a chaotic system in the phase space does not correspond to a simple geometrical object, but rather to a complex structure called *strange attractor*.

Let us remember that a periodic oscillation is represented by a closed curve in the phase space called *limit cycle*, see Fig. 4b. The origin of this term comes from the fact that the closed curve attracts all the trajectories from its neighborhood, which also explains the name *simple attractor*. The minimal dimension of the phase space for a limit cycle oscillator is two, but this is not enough for chaotic motion to take place, since trajectories cannot intersect each other. A chaotic motion needs at least three dimensions. The Rössler model has exactly three dimensions and its numerical integration shows that this system lies on a strange attractor, see Fig. 4d. In the context of coupled chaotic systems many different synchronization states have been studied. In the present work, we have chosen to use strong coupling in order to make the states of both oscillators identical. As a result, the signals coincide and we obtain a regime of *complete synchronization*. But, we have to pay attention to how strong is the coupling, for example, if we consider two oscillators that are mechanically coupled with a rigid link, we can not speak of synchronization because the coupling imposes too strong limitations on the motion of the two systems. To determine what can be considered as a weak or a strong coupling is rather difficult, but we can say that the introduction of coupling should not qualitatively change the behavior of the interacting systems. The motion of the attractor exhibits the sensitive dependence on initial conditions. As mentioned before this means that two trajectories starting very close together will rapidly diverge from each other, and thereafter have totally different futures. The growth rate is called *Lyapunov exponent*. Consider the trajectories $x(k)$ and $y(k)$, starting, respectively, from $x(0)$ and $y(0)$. If both trajectories are, until time k, always in the same linear region, we can write

$$|x(j+1) - y(j+1)| = |f'(x(j))||x(j) - y(j)|, \quad j = 0, 1, ..., k-1 \tag{3}$$

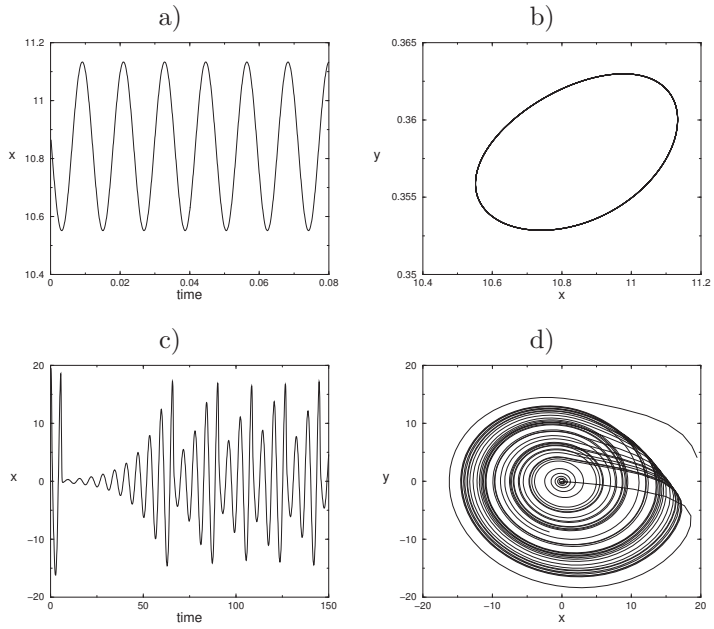

Figure 4: a) and b) Periodic oscillation is represented by a closed curve in the phase space. c) The Rössler's attractor. d) For the variables x, y the dynamics of the Rössler model look like rotations around the center, with irregular amplitude and an irregular return time.

where $f'(x)$ denotes the derivative of f at x. Thus,

$$|x(k) - y(k)| = |f'(x(k-1))||f'(x(k-2))| \dots |f'(x(0))||x(0) - y(0)| \tag{4}$$

or equivalently

$$|x(k) - y(k)| = e^{\lambda k}|x(0) - y(0)| \tag{5}$$

where

$$\lambda = \frac{1}{k}\sum_{j=0}^{k-1} ln|f'(x(j))|. \tag{6}$$

The equation (6) defines the Lyapunov exponent of the trajectory $x(k)$.
The interpretation of (5) is that λ gives the average rate of divergence (if $\lambda > 0$), or convergence (if $\lambda < 0$) of the two trajectories from each other, during the time interval $[0, k]$.

The scope of this work

The first objective of the present study is to calculate the evolution of the flow and heat transport patterns in a Hele-Shaw cell uniformly heated from below, from the onset of convection to relatively high Rayleigh numbers ($Ra \simeq 30Ra_c$). Having found the Rayleigh number's value from which the chaotic regime begins ($Ra = 1100$), the main purpose is to achieve the synchronization between two identical Hele-Shaw

cells laying in the chaotic regime.

A mathematical formulation of the modeling of the flow in a Hele-Shaw cell is proposed in Chapter 1. The configuration, which we have modeled consists in a box of porous material heated uniformly from below. It is a bounded two-dimensional square porous layer of thickness (height) h. The vertical boundaries are considered adiabatic. The horizontal top and bottom are isothermal, with the bottom warmer than the top, see Fig. 2. When no motion occurs, a vertical linear temperature distribution is set in the system.
The Chapters 2 and 3 are dedicated to explain the different numerical procedures that can be used to calculate the evolution of the temperature and velocity in the box. In order to integrate the flow during a long period in time, we propose a set of numerical methods, which permit to compute in an accurate and stable way the time evolution of the system. In chapter 2 we discuss the discretization of initial-value problems, considering, more specifically the advection-diffusion equations. One-step and multistep methods are considered for explicit and implicit schemes, paying special attention to the accuracy and stability of discretization. Chapter 3 is devoted to solve boundary value problems, essentially the Poisson, or more generally, Helmholtz equations. Also, in this case we offer different methods to find solutions in a rapid way, underlaying the success of the Fourier transform algorithms (FFT).
In chapter 4, we describe the results of the numerical integrations. We give the Rayleigh numbers that separate the different dynamical regimes. We describe the characteristics of the convective patterns after each transition, and analyze their effects on the heat transport through the analysis of the Nusselt number.
In the last chapter, after a brief discussion over what determines the spatial structures of the flow, we investigate possible synchronization mechanisms between two Hele-Shaw cells. Using a weak bidirectional thermal coupling between all the points of the two systems, we obtain the complete coincidence of the states. We also investigate the minimal number of points necessary to get synchronization and also the possibility of coupling both systems only through the lateral walls.

Chapter 1

Mathematical Formulation

1.1 Governing equations

A porous medium is a material consisting of a solid matrix with an interconnected void [12; 13]. The interconnectedness of the void (the pores) allows the flow of one or more fluids through the material.
In a natural porous medium the distribution of pores with respect to shape and size is irregular. On the pore scale (the microscopic scale) the flow quantities will be irregular, but many of these quantities are measured over areas that cross many pores, and such space-averaged (macroscopic) quantities change in a regular manner with respect to space and time.
The usual way of deriving the laws governing the macroscopic variables is to begin with the standard equations obeyed by the fluid [27; 28] and to obtain the macroscopic equations by averaging over volumes or areas containing many pores. In the textbook "Convection in Porous Media" [13] the authors construct a continuum model for a porous medium using a spatial approach: a macroscopic variable is defined over a sufficiently large representative elementary volume (r.e.v.). The value of the variable is evaluated in center of the volume and it is assumed that the result is independent of the size of the r.e.v.
In our problem, we will consider a bounded two-dimensional square porous layer of thickness h. The vertical boundaries are adiabatic. The horizontal boundaries are isothermal. The temperature difference across the porous layer is $\Delta T = T_0 - T_1$, the porous layer is heated from below. Let us briefly recall what are the governing equations for such system:
Conservation of mass.
The expression for the continuity equation for a flow through porous media is given by:

$$\phi \frac{\partial \rho_f}{\partial t} + \nabla \cdot (\rho_f \mathbf{v}) = 0, \tag{1.1}$$

where ρ_f is the fluid density, $\mathbf{v}$ is the fluid velocity and ϕ is the porosity of the porous medium, defined as the fraction of the total volume of the medium that is occupied by void space.
Conservation of momentum.

The usual Navier-Stokes equation is replaced by the Darcy's law which is assumed to describe the flow. The Darcy's law expresses proportionality between the flow rate and the applied pressure difference:

$$\nabla p = -\frac{\mu}{k}\mathbf{v}, \tag{1.2}$$

where ∇p is the pressure gradient in the flow direction, μ is the dynamic viscosity of the fluid and k is the permeability of the medium.
An extension of the equation (1.2) for the conservation of the momentum can be expressed in the following way:

$$\rho_f \left(\phi^{-1} \frac{\partial \mathbf{v}}{\partial t} + \phi^{-2} (\mathbf{v} \cdot \nabla)\mathbf{v} \right) = \rho_f \mathbf{g} - \nabla p - \frac{\mu}{k}\mathbf{v}, \tag{1.3}$$

where $\mathbf{g}$ is the acceleration due to gravity [12].
Conservation of energy.

$$(\phi(\rho c)_f + (1-\phi)(\rho c)_s) \frac{\partial T}{\partial t} + (\rho c)_f \mathbf{v} \cdot \nabla T = \lambda \nabla^2 T, \tag{1.4}$$

where $(\rho c)_s$ and $(\rho c)_f$ are respectively the heat capacity of the solid material and of the fluid and λ is the thermal conductivity of the fluid-saturated porous medium. Since ϕ is small for most relevant systems, the energy equation can be reduced to

$$\sigma \frac{\partial T}{\partial t} + \mathbf{v} \cdot \nabla T = \kappa \nabla^2 T, \tag{1.5}$$

where $\sigma = (\rho c)_s/(\rho c)_f$ is typically near unity and κ is the thermal diffusivity of the fluid-saturated porous medium. In the following we will assume $\sigma = 1$.

For thermal convection to occur, the density of the fluid must be a function of the temperature, hence we need an equation of state to complement the equations of mass, momentum and energy. The simplest equation of state is:

$$\rho_f = \rho_0[1 - \alpha(T - T_0)], \tag{1.6}$$

where ρ_0 is the fluid density at some reference temperature T_0 and the positive constant α is the thermal expansion coefficient. Equation (1.6) is obtained from the first term of the Taylor expansion of the equation of state of $\rho = \rho(p, T)$ in which the pressure variations are neglected.
It is usual in convection problems to invoke the Boussinesq's approximation. This consists of setting constant all properties of the medium, except the one that involves the buoyancy term, hence α is retained in the momentum equation. As a consequence the equation of continuity reduces to $\nabla \cdot \mathbf{v} = 0$. The Boussinesq's approximation is valid as long as that density changes remain small in comparison with ρ_0, and provided that the temperature variations are insufficient to vary the properties of the medium from their mean values.
Also the momentum equation may be simplified further by comparing the relative magnitude of the separate terms. Using this argument the equation (1.3) reduces to

$$\mathbf{v} = \frac{k}{\mu}(-\nabla p + \rho_f \mathbf{g}). \tag{1.7}$$

1.1.1 Stream function equation reformulation

As an alternative way of solving the governing equations in primitive variables, it is also possible to avoid the explicit appearance of the pressure by using the stream function formulation.
In two dimensions the governing equations are:

$$\begin{aligned} \frac{\partial u}{\partial x} + \frac{\partial v}{\partial y} &= 0, && (1.8)\\ \frac{\partial p}{\partial x} + \frac{\mu}{k}u &= 0, && (1.9)\\ \rho_0[1-\alpha(T-T_0)]g + \frac{\partial p}{\partial y} + \frac{\mu}{k}v &= 0, && (1.10)\\ \frac{\partial T}{\partial t} + u\frac{\partial T}{\partial x} + v\frac{\partial T}{\partial y} &= \kappa\left(\frac{\partial^2 T}{\partial x^2} + \frac{\partial^2 T}{\partial y^2}\right). && (1.11) \end{aligned}$$

In order to remove the pressure variable, we derive equation (1.10) with respect to x and subtract the derivative of equation (1.9) with respect to y. The resulting equation is:

$$-\alpha\rho_0 g\frac{\partial T}{\partial x} + \frac{\mu}{k}\left(\frac{\partial v}{\partial x} - \frac{\partial u}{\partial y}\right) = 0. \quad (1.12)$$

In two dimensions the stream function is defined by:

$$u = \frac{\partial \psi}{\partial y} \quad ; v = -\frac{\partial \psi}{\partial x}. \quad (1.13)$$

Using the stream-function formulation the equations become:

$$\begin{aligned} \nabla^2\psi &= -\frac{\alpha g k \rho_0}{\mu}\frac{\partial T}{\partial x},\\ \frac{\partial T}{\partial t} + \frac{\partial \psi}{\partial y}\frac{\partial T}{\partial x} - \frac{\partial \psi}{\partial x}\frac{\partial T}{\partial y} &= \kappa\left(\frac{\partial^2 T}{\partial x^2} + \frac{\partial^2 T}{\partial y^2}\right). && (1.14) \end{aligned}$$

The equations may now be expressed in dimensionless form, by introducing the new dimensionless variables:

$$\begin{aligned} \tilde{t} &= \frac{h^2}{\kappa}t\\ \tilde{\mathbf{x}} &= \frac{\mathbf{x}}{h}\\ \tilde{\mathbf{u}} &= \frac{h}{\kappa}\mathbf{u}\\ \tilde{\psi} &= \frac{\psi}{\kappa}\\ \tilde{T} &= \frac{T}{T_1 - T_0} = \frac{T}{\Delta T} && (1.15) \end{aligned}$$

after which the equations become:

$$\begin{aligned} \frac{\partial \tilde{T}}{\partial \tilde{t}} &= \nabla^2 \tilde{T} + \frac{\partial \tilde{\psi}}{\partial \tilde{y}} \frac{\partial \tilde{T}}{\partial \tilde{x}} - \frac{\partial \tilde{\psi}}{\partial \tilde{x}} \frac{\partial \tilde{T}}{\partial \tilde{y}}, \\ \nabla^2 \tilde{\psi} &= -Ra \frac{\partial \tilde{T}}{\partial \tilde{x}}, \end{aligned} \tag{1.16}$$

where Ra is the Rayleigh number and is defined by:

$$Ra = \frac{\alpha g k \rho_0 h \Delta T}{\mu \kappa}, \tag{1.17}$$

this number is a dimensionless parameter that measures the applied temperature difference. For an infinitely horizontally extended porous medium, the linear theory gives a Rayleigh number equals at the onset of convection to $4\pi^2$ (Lapwood [15]).

In this thesis, we have considered isothermal conditions at the lower and at the upper boundaries:

$$\tilde{T}(\tilde{x}, 0) = T_0 = 1 \quad \tilde{T}(\tilde{x}, 1) = T_1 = 0, \tag{1.18}$$

and adiabatic conditions at the lateral walls:

$$\frac{\partial \tilde{T}}{\partial \tilde{x}}(0, \tilde{y}) = \frac{\partial \tilde{T}}{\partial \tilde{x}}(1, \tilde{y}) = 0. \tag{1.19}$$

The stream-function vanishes at all boundaries as a result of the impermeability of the walls. In the following, in order to make the notation lighter, tildes are omitted but all variables are dimensionless.

1.1.2 The Nusselt number

An important consequence of convective motions is the increase of the heat flux q through the layer. Below the onset of convection $\Delta T < \Delta T_c$, and q is only due to conduction, $q = q_{cond}$. In contrast, when the fluid motion is present, the fluid velocity entails a supplementary heat flux q_{conv}, and then the total heat flux $q = q_{cond} + q_{conv}$ is higher than it would be in a purely conductive state.
This is expressed by the Nusselt number:

$$Nu = \frac{q_{cond} + q_{conv}}{q_{cond}}. \tag{1.20}$$

Hence $Nu = 1$ provided that $Ra < Ra_c$. For $Ra > Ra_c$ the Nusselt number increases reflecting the increasing part of the convection in the heat transport.
For a layer internally heated from below:

$$Nu = -\int_0^1 \frac{\partial T}{\partial y}|_{y=0} dx. \tag{1.21}$$

It can be easily checked, by substitution of the linear temperature profile in (1.21), that the reference value is given by $Nu = 1$ (for conduction).

Chapter 2

Solutions of Diffusive Initial Value Problems

Rayleigh-Bénard convection is so important that many numerical methods have been developed and tried over the years although [29; 30], somewhat unfortunately, most of these methods have not been compared with each other to determine which best achieves a practical balance of efficiency, accuracy, ease of programming, and parallel scalability on some specific computer architecture. Because our interest is to study fundamental questions in simple cell geometries, we chose not to use finite element [31; 32] or spectral methods [33; 34; 35] whose main strengths are the ability to handle irregular boundaries. In the present thesis, we have chosen second order accurate finite difference approximations.

2.1 Grid based methods and simple finite differences

The basic idea of a finite difference procedure [36; 37; 38] is to replace the continuous problem domain with a finite-difference mesh containing a finite number of grid points. In order to represent a function f on a two-dimensional domain spanned by Cartesian coordinates (x, y), we use $f(j\Delta x, i\Delta y)$. The grid points are located according to values of i and j, so difference equations are usually written in terms of the general point (j, i) and its neighbors.
The standard approach for approximating the differentials comes from truncated Taylors series [39; 40]. Consider a function $f(x, t)$ at a fixed time t. If f is sufficiently continuous in space we can expand it around any point $f(x + \Delta x)$ as

$$\begin{aligned} f(x+\Delta x) &= f(x) + \Delta x \frac{\partial f}{\partial x}(x) + \frac{(\Delta x)^2}{2}\frac{\partial^2 f}{\partial x^2}(x) + ... \\ &+ \frac{(\Delta x)^{n-1}}{(n-1)!}\frac{\partial^{n-1} f}{\partial x^{n-1}}(x) + \frac{(\Delta x)^n}{n!}\frac{\partial^n f}{\partial x^n}(\xi) \quad x \le \xi \le x + \Delta x \end{aligned} \tag{2.1}$$

where the last term can be identified as the remainder. If we ignore in this series terms of order Δx^2 and higher, we could approximate the first derivative at any point x_0 as

$$\frac{\partial f}{\partial x}(x_0) \approx \frac{f(x_0 + \Delta x) - f(x_0)}{\Delta x} + O(\Delta x) \tag{2.2}$$

where the last term is called the truncation error and it is the difference between the actual partial derivative and its finite-difference representation.
If we consider that our function is now stored in a discrete array of points f_j and $x = j\Delta x$ where Δx is the grid spacing, then at time step n we can write

$$\frac{\partial f}{\partial x}(x_0) \approx \frac{f_{j+1}^n - f_j^n}{\Delta x} + O(\Delta x) \tag{2.3}$$

where $(f_{j+1}^n - f_j^n)/\Delta x$ is the finite difference representation for $(\partial f/\partial x)_j$.
An identical procedure but expanding in time gives

$$\frac{\partial f}{\partial t}(t_0) \approx \frac{f_j^{n+1} - f_j^n}{\Delta t} + O(\Delta t) \tag{2.4}$$

Both of these approximations are however first order accurate as the leading term in the truncation error is of order Δx or Δt.

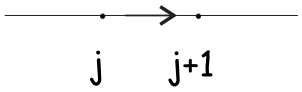

Figure 2.1: Forward space step.

2.1.1 Higher order finite difference schemes

In equation (2.1), we have considered the value of our function at one point forward in Δx. We could just have easily taken a step backward to get

$$f(x - \Delta x) = f(x) - \Delta x \frac{\partial f}{\partial x}(x_0) + \frac{(\Delta x)^2}{2} \frac{\partial^2 f}{\partial x^2}(x_0) + O(\Delta x^3) \tag{2.5}$$

If we truncate at order Δx^2 and above we still get a first order approximation

$$\frac{\partial f}{\partial x}(x_0) \approx \frac{f_j^n - f_{j-1}^n}{\Delta x} + O(\Delta x) \tag{2.6}$$

which is not any better than the forward step as it has the same order error (but of opposite sign). An improved scheme is obtained by combining equation (2.1) and (2.5) to remove the equal but opposite second order terms. If one subtracts (2.5) from (2.1) one gets the centered space approximation

$$\frac{\partial f}{\partial x}(x_0) \approx \frac{f_{j+1}^n - f_{j-1}^n}{2\Delta x} + O(\Delta x^2) \tag{2.7}$$

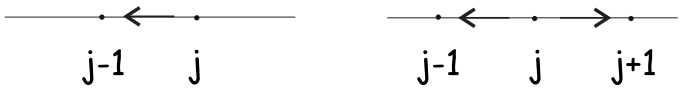

Figure 2.2: Backward and centered space step.

Note that we have still two grid points to approximate the derivative but we have gained an order of magnitude in the truncation error. By including more and more neighboring points, even higher order schemes can be obtained.
After considering the first derivative, we have also to consider an approximation for the second derivative. This time by adding (2.1) and (2.5) and rearranging we get

$$\frac{\partial^2 f}{\partial x^2}(x_0) \approx \frac{f^n_{j+1} - 2f^n_j + f^n_{j-1}}{(\Delta x)^2} + O(\Delta x^2) \tag{2.8}$$

This approximation only requires a point and its two neighbors.

2.1.2 Multi-dimensions

What we have done in one dimension in the first section, we generalize it to multi-dimension. Consider, for example, a function $f(x, y, t)$ at fixed time t and fixed point y. If f is continuous in space we can expand it again around any point $f(x + \Delta x, y)$ or $f(x, y + \Delta y)$. So if we ignore terms of order Δx^2 and Δy^2, and higher, and store the function in a discrete matrix of points $f_{i,j}$ where $x = j\Delta x$ and $y = i\Delta y$ are the grid spacings, at time steps n, we can write

$$\frac{\partial f}{\partial x}(x_0, y_0) \approx \frac{f^n_{i,j+1} - f^n_{i,j-1}}{2\Delta x} + O(\Delta x^2) \tag{2.9}$$

or

$$\frac{\partial f}{\partial y}(x_0, y_0) \approx \frac{f^n_{i+1,j} - f^n_{i-1,j}}{2\Delta y} + O(\Delta y^2) \tag{2.10}$$

at any point (x_0, y_0). In the same way, we can obtain an approximation for the second derivatives

$$\frac{\partial^2 f}{\partial x^2}(x_0, y_0) \approx \frac{f^n_{i,j+1} - 2f^n_{i,j} + f^n_{i,j-1}}{(\Delta x)^2} + O(\Delta x^2) \tag{2.11}$$

or for example

$$\frac{\partial^2 f}{\partial x \partial y}(x_0, y_0) \approx \frac{f^n_{i+1,j+1} - f^n_{i-1,j+1} - f^n_{i+1,j-1} + f^n_{i-1,j-1}}{4\Delta x \Delta y} + O(\Delta x^2) + O(\Delta y^2) \tag{2.12}$$

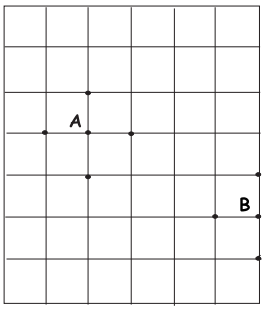

Figure 2.3: The second derivatives at the point A are evaluated using the points to which A is shown connected. The second derivatives at the point B are evaluated using the connected points and also using "right-hand-side" boundary information, as shown schematically.

2.2 Numerical solutions of the diffusion equation

Let us consider the two-dimensional diffusion equation:

$$\frac{\partial T}{\partial t} = \nabla^2 T. \tag{2.13}$$

We will begin considering how to solve the diffusion equation numerically by deriving some finite difference approximations to the Laplacian term [29; 38; 41; 42]. Given a 2-D square grid, we will use i and j to number the grid lines in the y and the x directions, respectively, with $i, j = 0, ..., N$ and $\Delta y = \Delta x = \Delta$.
Accordingly with last section, we represent the Laplacian as

$$\nabla^2 T = \frac{T_{i+1,j} - 2T_{i,j} + T_{i-1,j}}{\Delta^2} + \frac{T_{i,j+1} - 2T_{i,j} + T_{i,j-1}}{\Delta^2} \tag{2.14}$$

which is a second-order accurate approximation.
For convenience and future notation, it is useful to write (2.14) as

$$\nabla^2 T = \frac{1}{\Delta x^2} \begin{bmatrix} & 1 & \\ 1 & -2 & 1 \\ & 1 & \end{bmatrix} T_{i,j} + \frac{1}{\Delta y^2} \begin{bmatrix} & 1 & \\ 1 & -2 & 1 \\ & 1 & \end{bmatrix} T_{i,j} \tag{2.15}$$

which is an operator that acts on a point $T(i, j)$ and its two nearest neighbors and it is represented by a tridiagonal matrix that is primarily zero except for the diagonal (which has value -2) and the super- and sub-diagonal (of value 1).
Given a discretization of the thermal diffusion term we still need to add the time derivative for the left-hand-side. Using a forward time step the approximation of the diffusion equation can be written

$$\frac{T^{n+1}_{i,j} - T^n_{i,j}}{\Delta t} = \frac{T^n_{i+1,j} - 2T^n_{i,j} + T^n_{i-1,j}}{\Delta^2} + \frac{T^n_{i,j+1} - 2T^n_{i,j} + T^n_{i,j-1}}{\Delta^2} \tag{2.16}$$

or, in matrix form

$$\begin{aligned}
\frac{T_{i,j}^{n+1} - T_{i,j}^{n}}{\Delta t} &= \frac{1}{\Delta^2} \begin{bmatrix} & 1 & \\ 1 & -4 & 1 \\ & 1 & \end{bmatrix} T_{i,j}^{n} \\
T_{i,j}^{n+1} &= T_{i,j}^{n} + \alpha \begin{bmatrix} & 1 & \\ 1 & -4 & 1 \\ & 1 & \end{bmatrix} T_{i,j}^{n} \\
T_{i,j}^{n+1} &= \begin{bmatrix} & \alpha & \\ \alpha & 1-4\alpha & \alpha \\ & \alpha & \end{bmatrix} T_{i,j}^{n} \qquad (2.17)
\end{aligned}$$

where

$$\alpha = \frac{\Delta t}{\Delta^2} \qquad (2.18)$$

physically corresponds to the number of grid points that heat reaches in a time step (or it is the inverse of the number of time step required for heat to diffuse a grid space) [43; 44].

2.2.1 Stability analysis

From the material presented thus far, it is evident that a variety of numerical schemes can be written, but they are not all equally acceptable. The difference representation given by (2.16) is referred to as the simple explicit scheme for the heat diffusion equation (Euler scheme). An explicit scheme is one for which only one unknown appears in the difference equation in a manner that permits evaluation in terms of known quantities.

The first requirement that any scheme should meet is that of stability. A stable scheme is defined as one for which errors from any source are not permitted to grow in the sequence of numerical procedures as the calculation proceeds from one step to the next.

The Von Neumann stability analysis is perhaps the most widely used for establishing the stability characteristics of a finite-difference scheme. Instead of considering the behavior of the truncated terms we will now consider the behavior of small sinusoidal errors. If S is the exact solution of the difference scheme, we suppose to have obtained $S + \delta$, where δ is the results of errors arising from any sources. If we substitute in the equation (2.16), S will cancel out because it satisfies the difference equation, we have

$$\frac{\delta_{i,j}^{n+1} - \delta_{i,j}^{n}}{\Delta t} = \frac{\delta_{i+1,j} - 2\delta_{i,j} + \delta_{i-1,j}}{\Delta^2} + \frac{\delta_{i,j+1} - 2\delta_{i,j} + \delta_{i,j-1}}{\Delta^2}. \qquad (2.19)$$

If the difference equation is linear, the errors will satisfy an equation of the same form as the original difference equation.

At each time step in the computation a group of errors is introduced. If $E(x, y)$ are the errors at $t = 0$, we can consider a harmonic decomposition of them

$$E(x, y) = \sum_m A_m e^{i\beta_m x} e^{i\gamma_m y} \tag{2.20}$$

where β and γ are respectively, the wave number in the x and y direction. Because the solution have to be stable for every β_m and γ_m, it is only necessary to consider a single error term $e^{i\beta x}e^{i\gamma y}$, where β and γ belong to β_m and γ_m. So, we find a solution such that it reduces to $e^{i\beta x}e^{i\gamma y}$ when $t = 0$. There is only one such solution

$$\delta(x, y, t) = e^{at} e^{i\beta x} e^{i\gamma y} \tag{2.21}$$

where a may be real or complex. Substituting the equation (2.40) in (2.33) gives

$$\begin{aligned} \frac{e^{a(t+\Delta t)} e^{i\beta x} e^{i\gamma y} - e^{at} e^{i\beta x} e^{i\gamma y}}{\Delta t} &= \frac{e^{at} e^{i\beta(x+\Delta x)} e^{i\gamma y} - 2e^{at} e^{i\beta x} e^{i\gamma y} + e^{at} e^{i\beta(x-\Delta x)} e^{i\gamma y}}{(\Delta x)^2} \\ &+ \frac{e^{at} e^{i\beta x} e^{i\gamma(y+\Delta y)} - 2e^{at} e^{i\beta x} e^{i\gamma y} + e^{at} e^{i\beta x} e^{i\gamma(y-\Delta y)}}{(\Delta y)^2} \end{aligned}$$

Solving for the error at $t + \Delta t$ gives

$$\begin{aligned} \delta(x, y, t + \Delta t) &= e^{a(t+\Delta t)} e^{i\beta x} e^{i\gamma y} \\ &= e^{at} e^{i\beta x} e^{i\gamma y} + \alpha_x (e^{at} e^{i\beta(x+\Delta x)} e^{i\gamma y} - 2e^{at} e^{i\beta x} e^{i\gamma y} + e^{at} e^{i\beta(x-\Delta x)} e^{i\gamma y}) \\ &+ \alpha_y (e^{at} e^{i\beta x} e^{i\gamma(y+\Delta y)} - 2e^{at} e^{i\beta x} e^{i\gamma y} + e^{at} e^{i\beta x} e^{i\gamma(y-\Delta y)}) \end{aligned}$$

The ratio of the error at $t + \Delta t$ to that at t, $\delta(x, y, t + \Delta t)/\delta(x, y, t)$, is know as the amplification factor G. The errors will not grow if $|G| < 1$, this is known as the Von Neumann condition. So, by dividing equation (2.42) by $\delta(x, y, t)$

$$\frac{\delta(x, y, t + \Delta t)}{\delta(x, y, t)} = e^{a\Delta t} = 1 + \alpha_x (e^{i\beta\Delta x} - 2 + e^{-i\beta\Delta x}) + \alpha_y (e^{i\gamma\Delta y} - 2 + e^{-i\gamma\Delta y}) \tag{2.22}$$

Making use of the identity $e^{iz} = cos(z) + isin(z)$ the equation (2.42) can be written in the following way

$$e^{a\Delta t} = 1 + 2\alpha_x [cos(\beta\Delta x) - 1] + 2\alpha_y [cos(\gamma\Delta y) - 1] \tag{2.23}$$

Requiring that $|G| = |e^{a\Delta t}|$ be less than or equal to 1 gives

$$|1 + 2\alpha_x [cos(\beta\Delta x) - 1] + 2\alpha_y [cos(\gamma\Delta y) - 1]| \leq 1 \tag{2.24}$$

that using the half-angle identity became

$$|1 - 4\alpha_x sin^2 \frac{\beta\Delta x}{2} - 4\alpha_y sin^2 \frac{\gamma\Delta y}{2}| \leq 1. \tag{2.25}$$

If

$$1 - 4\alpha_x sin^2 \frac{\beta\Delta x}{2} - 4\alpha_y sin^2 \frac{\gamma\Delta y}{2} \geq 0 \tag{2.26}$$

that is

$$-4\alpha_x sin^2\frac{\beta\Delta x}{2} - 4\alpha_y sin^2\frac{\gamma\Delta y}{2} \leq 0 \tag{2.27}$$

the inequality is always satisfied because $\alpha > 0$. Whereas if

$$1 - 4\alpha_x sin^2\frac{\beta\Delta x}{2} - 4\alpha_y sin^2\frac{\gamma\Delta y}{2} < 0 \tag{2.28}$$

that is

$$\alpha_x sin^2\frac{\beta\Delta x}{2} + \alpha_y sin^2\frac{\gamma\Delta y}{2} \leq \frac{1}{2} \tag{2.29}$$

the inequality is satisfied if

$$\alpha_x + \alpha_y \leq \frac{1}{2}. \tag{2.30}$$

If $\Delta x = \Delta y$ the condition (2.30) becomes

$$2\alpha \leq \frac{1}{2}. \tag{2.31}$$

This provides the stability requirement for this method. This means that a decrease in grid spacing, for example, by a factor of 2 in both direction requires a factor of 16 more computer time. In fact, this choice for Δx implies that the grid's point numbers is increased by a factor 4 and from the condition (2.31) it follows that the new Δt is four times smaller than the original time step. Unfortunately, because the simplest centered schemes are only second order in space (and first order in time), we gain only a factor of 4 in reducing the truncation error. Fortunately, this is not the only scheme available. We will develop implicit schemes which are unconditionally stable and we will can take as large a step as we want.

2.3 Implicit scheme and stability: Crank-Nicholson scheme

At the end of the last section we have shown that if we use an explicit scheme we have to choose time steps that satisfy the restriction (2.31). But, sometimes time steps comparable to, or smaller than, $(\Delta x)^2/4$ may be physically unreasonable. For this reason we will use a implicit scheme which is unconditionally stable.
In an explicit scheme we have only one unknown, since the parabolic heat equation governs a marching problem for which an initial distribution of T must be specified. The temperature field T at time level n can be considered to be known. If the second derivative term in the heat equation were approximated by the temperature field taken at the $n+1$ time level, three unknowns would appear in the difference equation. In this case the procedure is called implicit, indicating that the algebraic formulation would require the simultaneous solution of several equations involving the unknowns.
The simplest implicit scheme for the heat diffusion equation can be developed from the Taylor series by simply evaluating the heat diffusion term at the $n+1$ time level

(all we have to do is to rewrite equation (2.16) replacing the diffusion rate at time step n with that at time step $n+1$):

$$\frac{T_{i,j}^{n+1} - T_{i,j}^{n}}{\Delta t} = \frac{T_{i+1,j}^{n+1} - 2T_{i,j}^{n+1} + T_{i-1,j}^{n+1}}{\Delta^2} + \frac{T_{i,j+1}^{n+1} - 2T_{i,j}^{n+1} + T_{i,j-1}^{n+1}}{\Delta^2} \tag{2.32}$$

or, in matrix form

$$T_{i,j}^{n+1} = T_{i,j}^{n} + \alpha \begin{bmatrix} & 1 & \\ 1 & -4 & 1 \\ & 1 & \end{bmatrix} T_{i,j}^{n+1}. \tag{2.33}$$

This is an implicit method because we do not know in advance what the right-hand-side will evaluate to, however, we can again rearrange (2.33) to solve $T_{i,j}^{n+1}$ as

$$T_{i,j}^{n} = \begin{bmatrix} & -\alpha & \\ -\alpha & 1+4\alpha & -\alpha \\ & -\alpha & \end{bmatrix} T_{i,j}^{n+1} \tag{2.34}$$

This scheme is first order accurate in time and second order accurate in space.
The Von Neumann method can easily be applied to this scheme to determine its stability characteristics. Proceeding in the same way that for the explicit scheme, we obtain that the error satisfy an equation of the same form as equation (2.32). Substituting $\delta(x,y,t) = e^{at}e^{i\beta x}e^{i\gamma y}$ into that equation and requiring that $|G| \leq 1$ gives

$$|G| = \left(1 + 4\alpha sin^2\frac{\beta\Delta x}{2} + 4\alpha sin^2\frac{\gamma\Delta y}{2}\right)^{-1} \leq 1 \tag{2.35}$$

which is satisfied for any $\alpha \geq 0$. So, the difference equation is effectively, unconditionally stable.
We can obtain a second order scheme in both space and time, simply averaging the explicit and implicit schemes:

$$\begin{aligned} \frac{T_{i,j}^{n+1} - T_{i,j}^{n}}{\Delta t} &= \frac{1}{2}\left(\frac{(T_{i+1,j}^{n+1} - 2T_{i,j}^{n+1} + T_{i-1,j}^{n+1}) + (T_{i+1,j}^{n} - 2T_{i,j}^{n} + T_{i-1,j}^{n})}{\Delta^2}\right) \\ &+ \frac{1}{2}\left(\frac{(T_{i,j+1}^{n+1} - 2T_{i,j}^{n+1} + T_{i,j-1}^{n+1}) + (T_{i,j+1}^{n} - 2T_{i,j}^{n} + T_{i,j-1}^{n})}{\Delta^2}\right) \end{aligned} \tag{2.36}$$

Here both the left- and the right-hand sides are centered at time step $n+1/2$, so the method is second-order accurate in time, as we said. This scheme is called *Crank-Nicholson* scheme and it is also unconditionally stable.
Inspection of (2.36), shows that Crank-Nicholson in one dimension is a system of linear equations of the form

$$\mathbf{Ax} = \mathbf{b} \tag{2.37}$$

where $\mathbf{A}$ is a tridiagonal matrix that is primarily zero except for the diagonal (which has value $(1+4\alpha)$) and one super and sub diagonal (of value $-\alpha$). For (2.37) the

vector $\mathbf{x}$ corresponds to the matrix of the temperature values at the time step $n+1$, $\mathbf{T}^{n+1}$, and the vector $\mathbf{b}$ is the known temperature at time n. So, we want solve

$$\mathbf{A}\mathbf{T}^{n+1} = \mathbf{T}^n \tag{2.38}$$

$\mathbf{A}$ is a symmetric and positive definite matrix, so it can be inverted. Tridiagonal matrix can be inverted in order N operations where N is the total number of grid points. The IMSL library provides efficient implementations of tridiagonal solvers and shows that tridiagonal algorithm makes the implicit methods very competitive for the heat diffusion equation in terms of computational effort.
Unfortunately in two dimensions this scheme is no longer tridiagonal. In fact the extension of the Crank-Nicholson scheme (to two dimensions) leads to a system of linear equations that contains five unknowns for two dimensions. It looks like

$$\begin{bmatrix} & -1 & \\ -1 & 2(2+\alpha) & -1 \\ & -1 & \end{bmatrix} T^{n+1} = \begin{bmatrix} & 1 & \\ 1 & 2(2-\alpha) & 1 \\ & 1 & \end{bmatrix} T^n \tag{2.39}$$

equation (2.39) is a "band" tridiagonal system of simultaneous linear equations and the inversion of the matrix in this case is significant more expensive computationally. However the scheme remains unconditionally stable. One possibility to solve them is use a sparse matrix technique, or another approach, which combines second order accuracy in space and time with the ease of tridiagonal solvers, is the Alternating-Direction Implicit scheme.

2.3.1 Alternating-Direction Implicit scheme

One possibility is to use the ADI scheme, the idea is split one process into its different directional components. For example, we could rewrite our multidimensional diffusion equation as

$$\frac{\partial T}{\partial t} = \mathcal{L}_x T + \mathcal{L}_y T \tag{2.40}$$

where $\mathcal{L}_x$ is the operator controlling diffusion in the horizontal direction and $\mathcal{L}_y$ controls diffusion in the vertical direction. Given this splitting, ADI schemes then solve (2.40) by taking two-passes, first solving an implicit diffusion equation in the horizontal for the first half time step and then an implicit diffusion equation in the vertical for the second half time step.
In more detail, the ADI algorithm for (2.13) looks like

$$\begin{aligned} \frac{T_{i,j}^{n+\frac{1}{2}} - T_{i,j}^{n}}{\Delta t/2} &= \frac{1}{\Delta x^2}\left(T_{i+1,j}^{n+\frac{1}{2}} - 2T_{i,j}^{n+\frac{1}{2}} + T_{i-1,j}^{n+\frac{1}{2}}\right) \\ &+ \frac{1}{\Delta y^2}\left(T_{i,j+1}^{n} - 2T_{i,j}^{n} + T_{i,j-1}^{n}\right) \end{aligned} \tag{2.41}$$

$$\begin{aligned} \frac{T_{i,j}^{n+1} - T_{i,j}^{n+\frac{1}{2}}}{\Delta t/2} &= \frac{1}{\Delta x^2}\left(T_{i+1,j}^{n+\frac{1}{2}} - 2T_{i,j}^{n+\frac{1}{2}} + T_{i-1,j}^{n+\frac{1}{2}}\right) \\ &+ \frac{1}{\Delta y^2}\left(T_{i,j+1}^{n+1} - 2T_{i,j}^{n+1} + T_{i,j-1}^{n+1}\right) \end{aligned} \tag{2.42}$$

Only one tridiagonal system of equations must be solved for each half step. The equation (2.42) is an implicit, tridiagonal equation for the horizontal rows at time $n+1/2$ which are then used in the equation (2.42) to update the vertical columns at time $n+1$. The tridiagonal nature of these two schemes can be made more apparent if we collect terms of the same time step together. For a uniform grid we can rewrite the equations (2.42) as

$$[-1 \quad \alpha+2 \quad -1]T^{n+\frac{1}{2}} = \begin{bmatrix} 1 \\ \alpha-2 \\ 1 \end{bmatrix} T^n$$

$$\begin{bmatrix} -1 \\ \alpha+2 \\ -1 \end{bmatrix} T^{n+1} = [1 \quad \alpha-2 \quad 1]T^{n+\frac{1}{2}} \tag{2.43}$$

where a horizontal stencil implies horizontal neighbors and vertical stencil implies vertical neighbor.
The advantage of this method is that each time step requires only the solution of two simple tridiagonal systems.

2.4 The non-linear term

Our diffusion equation is not linear, it has the following form

$$\frac{\partial T}{\partial t} = \nabla^2 T + J, \tag{2.44}$$

where J is the Jacobian non linear term and in two dimensions it is written

$$J = \frac{\partial \psi}{\partial y}\frac{\partial T}{\partial x} - \frac{\partial \psi}{\partial x}\frac{\partial T}{\partial y} \tag{2.45}$$

this term is also known as the *advection term*. By studying the way to construct a computer model of the general circulation of the atmosphere, Arakawa [45] has explained that a simple finite difference approximation using central differences, for example

$$\frac{\partial \psi}{\partial y}\frac{\partial T}{\partial x} = \frac{(\psi_{i+1,j} - \psi_{i-1,j})\,(T_{i,j+1} - T_{i,j-1})}{4\Delta^2} \tag{2.46}$$

causes numerical instability. At first he thought his problems were "truncation error". A computer cannot produce numbers with infinite precision. When thousands of calculation are repeated and the numbers are truncated each time, we add up tiny discrepancies over and over. As result we have a big discrepancy. Eventually the solutions became unrealistic and "explode". But after that Arakawa recognized that the instability was like the problem of a platoon of soldiers ordered to march across a bridge. If they march across in step, it may happen that somewhere there is a combination that resonates at just the frequency of their marching. Each time the feet come down, they hit that combination at the same phase of its swing, pushing

it a little further. Soldiers know that bridges can resonate and they will break step before crossing.
Something like this happened with Arakawa's simulations. Suppose the computer goes through a complete step and takes its next step after a simulation interval of, for example, one hour. Among the simulated waves there would be some with a frequency of just one hour. Every time the calculation was repeated, the computer would catch those waves at the same phase (aliasing occurs when the sampling frequency is too low with respect to the frequency content in the original time series. A new, but false frequency is obtained by the sampling procedure). Arakawa sought a way to make the small pushes cancel one another out, as the impact of the feet of the soldiers would cancel one another if they broke step. The key, he found, was to write equations in such a way that certain quantities would remain unchanged. For example, the kinetic energy. In the real world, the law of conservation of energy demands that there is never any change in the total energy, whereas kinetic energy alone is not normally conserved. But by using equations that did conserve kinetic energy, Arakawa could make sure that no unrealistic spike of wind speed grew exponentially from his calculations.
To avoid aliasing errors Arakawa developed nine- and thirteen-point representations of the Jacobian J which conserve the kinetic energy and which have a truncation error of the square and fourth power, respectively, of the spatial difference x. These numerical schemes are known as the second and fourth-order Arakawa schemes.
We choose second order Arakawa scheme. There are different possibilities to write the expression for the Jacobian [46; 47]:

$$\begin{aligned} J(\psi,T) &= \frac{\partial\psi}{\partial y}\frac{\partial T}{\partial x}-\frac{\partial\psi}{\partial x}\frac{\partial T}{\partial y} \\ &= \frac{\partial}{\partial x}\left(\psi\frac{\partial T}{\partial y}\right)-\frac{\partial}{\partial y}\left(\psi\frac{\partial T}{\partial x}\right) \\ &= \frac{\partial}{\partial y}\left(T\frac{\partial\psi}{\partial x}\right)-\frac{\partial}{\partial x}\left(T\frac{\partial\psi}{\partial y}\right) \\ &= \frac{1}{2r}\left\{\left(\frac{\partial\psi}{\partial y}-r\frac{\partial\psi}{\partial x}\right)\left(\frac{\partial T}{\partial y}+r\frac{\partial T}{\partial x}\right)-\left(\frac{\partial T}{\partial y}-r\frac{\partial T}{\partial x}\right)\left(\frac{\partial\psi}{\partial y}+r\frac{\partial\psi}{\partial x}\right)\right\} \end{aligned}$$

The last expression follows from

$$\begin{aligned} \eta &= x-\frac{y}{r} \\ \xi &= x+\frac{y}{r} \end{aligned}$$

from which

$$\begin{aligned} \frac{\partial}{\partial\eta} &= \frac{1}{2}\left(\frac{\partial}{\partial x}-r\frac{\partial}{\partial y}\right), \\ \frac{\partial}{\partial\xi} &= \frac{1}{2}\left(\frac{\partial}{\partial x}+r\frac{\partial}{\partial y}\right), \end{aligned} \tag{2.47}$$

and

$$J(\psi,T)=\frac{2}{r}\left\{\frac{\partial\psi}{\partial y}\frac{\partial T}{\partial x}-\frac{\partial\psi}{\partial x}\frac{\partial T}{\partial y}\right\} \tag{2.48}$$

The resulting schemes will depend on the choice of the mathematical expression for the Jacobian. From the first expression we have

$$J^{++}=\frac{1}{4\Delta x\Delta y}\Big\{(\psi_{i,j+1}-\psi_{i,j-1})(T_{i+1,j}-T_{i-1,j})-(\psi_{i+1,j}-\psi_{i-1,j})(T_{i,j+1}-T_{i,j-1})\Big\},$$

from the second expression we get:

$$\begin{aligned}J^{+\times} &= \frac{1}{4\Delta x\Delta y}\Big\{\psi_{i,j+1}(T_{i+1,j+1}-T_{i-1,j+1})-\psi_{i,j-1}(T_{i+1,j-1}-T_{i-1,j-1})\\ &- \psi_{i+1,j}(T_{i+1,j+1}-T_{i+1,j-1})+\psi_{i-1,j}(T_{i-1,j+1}-T_{i-1,j-1})\Big\},\end{aligned} \tag{2.49}$$

the third one leads to:

$$\begin{aligned}J^{\times+} &= \frac{1}{4\Delta x\Delta y}\Big\{T_{i+1,j}(\psi_{i+1,j+1}-\psi_{i+1,j-1})-T_{i-1,j}(\psi_{i-1,j+1}-\psi_{i-1,j-1})\\ &- T_{i,j+1}(\psi_{i+1,j+1}-\psi_{i-1,j+1})+T_{i,j-1}(\psi_{i+1,j-1}-\psi_{i-1,j-1})\Big\},\end{aligned} \tag{2.50}$$

finally, from the last one with $r=\Delta y/\Delta x$:

$$\begin{aligned}J^{\times\times} &= \frac{1}{8\Delta x\Delta y}\Big\{(\psi_{i-1,j+1}-\psi_{i+1,j-1})(T_{i+1,j+1}-T_{i-1,j-1})\\ &- (\psi_{i+1,j+1}-\psi_{i-1,j-1})(T_{i-1,j+1}-T_{i+1,j-1})\Big\}.\end{aligned} \tag{2.51}$$

A viable form to represent the Jacobian is

$$J=aJ^{++}+bJ^{\times+}+cJ^{+\times}+dJ^{\times\times},\quad a+b+c+d=1 \tag{2.52}$$

In the discretized expression for the Jacobian J the two super-indices indicate the points where ψ and T are evaluated respectively. For example, $J^{+\times}$ means that ψ is evaluated in the adjacent horizontal and vertical points and T is evaluated with the neighboring points on the diagonals. In the present thesis, we have chosen to use $d=0$ and $a=b=c=1/3$ for the discretization of the Jacobian [17].

2.5 Multistep methods

The method proposed in section 2.3.1 is known as single-step because it uses information from only the last step computed. The value T_{ij}^{n+1} depends only on T_{ij}^{n}. It exists a class of methods that use past values for the approximation of the solution. They are known as multistep methods.

For ordinary differential equations the principle of multistep methods can be used for the solution of the initial value problem

$$\frac{dy}{dx} = f(x, y), \quad y(x_0) = y_0, \tag{2.53}$$

can be expressed in integral form as

$$y_{k+1} = y_k + \int_{x_k}^{x_{k+1}} f(x, y(x))dx, \tag{2.54}$$

where y_k,y_{k-1},...,y_{k-N} are approximations of the solution at x_k,x_{k-1},...,x_{k-N}, for some integer N. The integral on the right can be approximated by a numerical quadrature formula and the result will be a formula for generating the approximate solution step by step. There is a unique polynomial $p(x)$ of degree N such that $p(x_i) = f_i = f(x_i, y_i)$, for $i = k, ..., k - N$. So the explicit multistep method is:

$$y_{k+1} = y_k + \int_{x_k}^{x_{k+1}} p(x)dx. \tag{2.55}$$

If $N = 0$, we have just the Euler's method. If $N = 1$, p is a linear function connecting (x_k, f_k) and (x_{k-1}, f_{k-1}):

$$p_1(t) = f_k + \frac{1}{h}(x - x_k)(f_k - f_{k-1}). \tag{2.56}$$

Substituting (2.56) into (2.55), we have:

$$y_{k+1} = y_k + hf_k + \frac{h}{2}(f_k - f_{k-1}) = y_k + \frac{h}{2}(3f_k - f_{k-1}), \tag{2.57}$$

a two step method (see how it is modified with respect the Euler method).
If $N = 2$, the polynomial interpolating (x_k, f_k),(x_{k-1}, f_{k-1}),(x_{k-2}, f_{k-2}), is of tree form:

$$p_2(x) = p_1(x) + \frac{(x - x_k)(x - x_{k-1})}{2h^2}(f_k - 2f_{k-1} + f_{k-2}). \tag{2.58}$$

Evaluating the integral we find:

$$y_{k+1} = y_k + hf_k + \frac{h}{2}(f_k - f_{k-1}) + \frac{56}{6}(f_k - 2f_{k-1} + f_{k-2}), \tag{2.59}$$

a 3 step method modified from 2 step method (2.57). Completing the integration, we get:

$$y_{k+1} = y_k + \frac{h}{12}(23f_k - 16f_{k-1} + 5f_{k-2}). \tag{2.60}$$

Similarly, for $N = 3$, one has the 4 step method:

$$y_{k+1} = y_k + \frac{h}{24}(55f_k - 59f_{k-1} + 37f_{k-2} - 9f_{k-3}). \tag{2.61}$$

The above explicit multistep methods are called Adams-Bashforth methods of order $N + 1$.

2.5.1 ADI scheme revisited

By adding the non-linear term and using a second-order Adams-Bashforth method in the diffusion equation, the ADI scheme is modified as follow:

$$[-1 \quad \alpha+2 \quad -1]T^{n+\frac{1}{2}} = \begin{bmatrix} 1 \\ \alpha-2 \\ 1 \end{bmatrix} T^n - \tfrac{\Delta t}{2}\rho \tag{2.62}$$

$$\begin{bmatrix} -1 \\ \alpha+2 \\ -1 \end{bmatrix} T^{n+1} = [1 \quad \alpha-2 \quad 1]T^{n+\frac{1}{2}} - \tfrac{\Delta t}{2}\rho \tag{2.63}$$

where

$$\rho = \frac{1}{2}\left(3J(\psi^n, T^n) - J(\psi^{n-1}, T^{n-1})\right) \tag{2.64}$$

In the ADI scheme we have to solve two tridiagonal systems, one for each spatial directions at every time step. We have spoken yet about the implementation of boundary conditions. The equations (2.62) and (2.63) can be used to calculate the solution at the internal points, while the temperatures at the boundaries are supplied by the given boundary conditions.
In the first half step we have to solve the a implicit system in the x direction. In this case, the boundary condition that we have to consider are the condition at the lateral walls. We imposed a Neumann boundary condition that fixes the heat flux $(= 0)$ at the boundary

$$\frac{\partial T}{\partial x}(0, y) = \frac{\partial T}{\partial x}(1, y) = 0. \tag{2.65}$$

Hence we can obtain the temperature at the boundary by approximating the derivative in (2.65) by a finite difference. In sections 3.1 and 3.2, we have written a first approximation for the first derivative using only two points

$$\frac{\partial T_{i,0}}{\partial x} = \frac{T_{i,1} - T_{i,0}}{\Delta}; \qquad \frac{\partial T_{i,N}}{\partial x} = \frac{T_{i,N} - T_{i,N-1}}{\Delta}. \tag{2.66}$$

From (2.65) and (2.66) we deduce that

$$T_{i,0} = T_{i,1} \quad T_{i,N} = T_{i,N-1}. \tag{2.67}$$

A derivative using three points formula will increase the precision

$$\begin{aligned} \frac{\partial T_{i,0}}{\partial x} &= \frac{-3T_{i,0} + 4T_{i,1} - T_{i,2}}{2\Delta} \\ \frac{\partial T_{i,N}}{\partial x} &= \frac{T_{i,N-2} - 4T_{i,N-1} + 3T_{i,N}}{2\Delta} \end{aligned}$$

from which

$$T_{i,0} = \frac{4T_{i,1} - T_{i,2}}{3} \quad T_{i,N} = \frac{4T_{i,N-1} - T_{i,N-2}}{3}. \tag{2.68}$$

For the second half step in the vertical direction we consider the upper and lower boundaries, where Dirichlet boundary condition are imposed:

$$T_{0,j} = 1 \quad \text{at the bottom} \tag{2.69}$$

and

$$T_{N,j} = 0 \quad \text{at the top of the layer} \tag{2.70}$$

Chapter 3

Boundary Value Problem

In the previous section we have been concerned with time dependent initial value problems where we start with some assumed initial condition (plus appropriate boundary conditions), then we calculate how this solution will change in time. We have considered both implicit and explicit numerical schemes, but the basic point is that given a starting field it is relatively simple to get the next step. The principal difficulties with time dependent scheme are stability and accuracy.
In a boundary value problem we are trying to satisfy a steady state solution in space that agrees with our prescribed boundary conditions. In general, boundary value problems will reduce, when discretized, to a large and sparse set of linear equations. While stability is no more a problem, efficiency in solving these equations is important.
In the following sections we will describe several approaches for discretizing and solving elliptic (2nd order) boundary value problems. We will consider the simplest elliptic problem which is a Poisson problem of the form:

$$\nabla^2 u = f(x, y) \tag{3.1}$$

We have already discussed finite difference approximations in the previous sections on 2-D initial value problems. For boundary value problems, nothing has changed except that we do not have any time derivatives to deal with any more. For example, the standard 5-point discretization of the equation (3.1) on a regular 2-D cartesian mesh with uniform grid ($\Delta x = \Delta y = \Delta$) is:

$$\frac{1}{\Delta^2}(u_{i+1,j} - 2u_{i,j} + u_{i-1,j}) + \frac{1}{\Delta^2}(u_{i,j+1} - 2u_{i,j} + u_{i,j-1}) = f_{i,j} \tag{3.2}$$

Finally, a note about boundary conditions. For determining T it is necessary to specify the boundary conditions. In general boundary conditions add auxiliary information that modify the matrix or the right hand-side or both. However, there are many ways to implement the boundary conditions and these depend somewhat on the method of solution. In general, for Dirichlet boundary conditions, because matrix methods can be so expensive, the fewer points the better so one approach is just to solve the unknown interior points.

3.1 Iterative methods

Iterative methods [48; 49; 50] consists of repeated application of an algorithm that is usually relatively simple and these methods are particularly useful for systems in which roundoff errors may be a problem. Furthermore, iterative procedures can easily take advantage of the sparse nature of the coefficient matrices, on the other hand they are certain to converge only for systems having "diagonal dominance".
We are going to review briefly the main concepts of the iterative methods. The most straightforward approach to a iterative solution of a linear system is to rewrite the linear equations $Ax = b$ as a linear fixed-point iteration. One way to do this is to write $Ax = b$ as

$$x = (I - A)x + b \tag{3.3}$$

and to define the *Richardson iteration*

$$x_{k+1} = (I - A)x_k + b. \tag{3.4}$$

We will discuss more general method in which $\{x_k\}$ is given by

$$x_{k+1} = Mx_k + c. \tag{3.5}$$

In (3.5) M is a matrix called the *iteration matrix*. Iterative methods of this form are called *stationary iterative methods* because the transition from x_k to x_{k+1} does not depend on the history of the iteration.
There are ways to convert $Ax = b$ to a linear fixed-point iteration that are different from (3.4). Methods such as Jacobi and Gauss-Seidel are based on *splitting* of A of the form:

$$A = A_1 + A_2, \tag{3.6}$$

where A_1 is a nonsingular matrix constructed so that equations with A_1 as coefficient matrix is easy to solve. The $Ax = b$ is converted to the fixed-point problem

$$x = A_1^{-1}(b - A_2x). \tag{3.7}$$

In the next section we show two iterative schemes the Jacobi and the Gauss-Seidel iterative methods.

3.1.1 Classical methods: Jacobi and Gauss-Seidel

In this section we want illustrate the simplest iterative scheme called Jacobi scheme. This is certainly not the best scheme because it converges too slowly, but it is the basis for understanding the modern methods, which are always compared with it.
The Jacobi iteration uses the splitting

$$A_1 = D, \quad A_2 = L + U \tag{3.8}$$

where D is the diagonal part of A, L is the lower triangle of A with zeros on the diagonal and U is the upper triangle of A with zeros on the diagonal. This leads to the iteration matrix

$$-D^{-1}(L + U). \tag{3.9}$$

If superscripts n and $n+1$ denote two successive iterates, then we can express the Jacobi iteration for (3.1) concretely as

$$U^{n+1} = D^{-1}[f^n - (L+U)U^n]. \tag{3.10}$$

Note that D is diagonal and hence trivial to invert.
For the simple regular Poisson stencil

$$A_{ij} = \frac{1}{\Delta^2}\begin{bmatrix} & 1 & \\ 1 & -4 & 1 \\ & 1 & \end{bmatrix} \tag{3.11}$$

we can write the Jacobi scheme in stencil notation as

$$U^{n+1}_{i,j} = -\frac{1}{4}\left[\Delta^2 f^n_{i,j} - \begin{bmatrix} & 1 & \\ 1 & 0 & 1 \\ & 1 & \end{bmatrix} U^n_{i,j}\right] \tag{3.12}$$

What is the rate of convergence of the Jacobi method ? First of all, the iteration (3.10) converges if and only if the *spectral radius*, defined as the largest eigenvalue of the iterative matrix and denoted ρ_s, is less than one. In other words, the matrix $D^{-1}(L+U)$ is trying to reduce the errors in our guess U^n and those errors can always be decomposed into orthogonal eingevectors with the property that

$$D^{-1}(L+U)x = \lambda x \tag{3.13}$$

where x is the eingevector and λ is the eingevalue. If λ is not less than one, repeated iterations of the equation (3.10) will causes the error to grow and blow up. Even for non-exploding iteration schemes, however, the rate of convergence will be controlled by the largest eigenvalue. Unfortunately for most iteration matrices, the largest eigenvalue approaches unity as the number of points increase and thus simple scheme tends to converge quite slowly.
The number of iterations r required to reduce the overall error by a factor 10^{-p} is thus estimated by

$$r \approx \frac{pln10}{(-ln\rho_s)} \tag{3.14}$$

In general, the spectral radius goes asymptotically to one as the grid-size is increased, so that more iterations are required. For the 2D diffusion equation on a grid $N \times N$ with Dirichlet boundary conditions on all four sides, the asymptotic formula for large N turn out to be

$$\rho_s \approx 1 - \frac{\pi^2}{2N^2}. \tag{3.15}$$

The number of iterations r required to reduce the error by a factor of 10^{-p} is thus

$$r \approx \frac{2pN^2 ln10}{\pi^2} \approx \frac{1}{2}pN^2. \tag{3.16}$$

In other words the number of iteration is proportional to the number of mesh points. Since our problem has a 129×129 points, it is clear that the Jacobi scheme is only

of theoretical interest.
The Gauss-Seidel method corresponds to the matrix decomposition:

$$A_1 = D + L \quad A_2 = U \tag{3.17}$$

and the iteration matrix is

$$M = -(D + L)^{-1}U. \tag{3.18}$$

Note that A_1 is lower triangular, and hence $A_1^{-1}y$ is easy to compute for vectors y. Note also that, unlike Jacobi iteration, the iteration depends on the ordering of the unknowns, as it can easily check writing out (3.7) in components. One can show that the spectral radius of a Gauss-Seidel scheme is the square of that the Jacobi scheme so it converges in about a factor of two less time. The factor of two improvement in the number of iterations over the Jacobi method still leaves the method impractical.

3.2 Direct methods

Direct methods [50] are based on the factorization of the coefficient matrix. In the (hypothetical) absence of rounding errors, these methods produce the exact solution of a linear system after a finite number of arithmetic operations. One of the most elementary methods is the Cramer's rule. Unfortunately the number of operations required in the algorithm is approximately proportional to $(n + 1)!$, where n is the number of unknowns. For more than about three equations the use of Cramer's rule becomes impractical owing to excessive computational effort and is not recommended. Gaussian elimination is a very useful and efficient tool for solving many systems of algebraic equations. Although it is one of the earliest methods proposed for solving simultaneous linear equations, it remains among the most important algorithms in use today. Direct methods for solving certain systems of algebraic equations that are significantly faster than Gaussian elimination do exist. Unfortunately, none of them is completely general. That is, they are applicable only to the algebraic equations arising from a special class of differential equations and associated boundary conditions. The algorithms for fast direct procedures tend to be rather complicated and are not easily adapted to irregular domains or complex boundary conditions. One of the simplest fast direct methods is the error vector propagation, but roundoff errors tend to accumulate in this method, so it is limited in applicability to relatively small systems of equation. Two fast direct methods for the Poisson equation that are not limited by the accumulation of roundoff errors are the even-odd reduction method and the fast Fourier transform method [51; 52; 53].

3.3 Matrix diagonalization method

In this section we present a method to solve the Poisson equation that we have obtained modifying a numerical scheme developed by Lopez [54; 55; 56; 57] to study axisymmetric Navier-Stokes equations. The algorithm is based on the use of the

matrix diagonalization method [58].
Consider the the left-hand-side of the equation (3.2). We claim that it may be rewritten as the matrix-matrix product $(1/\Delta^2)TU$, where U is the N-by-N matrix of $u(i,j)$, and T is the familiar symmetric tridiagonal matrix, that in stencil form we have written:

$$T = \begin{bmatrix} & 1 & \\ 1 & -2 & 1 \\ & 1 & \end{bmatrix} \tag{3.19}$$

A formal proof requires the simple computation:

$$\begin{aligned} T(i,j)U(i,j) &= \sum_k T(i,k)U(k,j) \\ &= T(i,i-1)U(i-1,j) + T(i,j)U(i,j) + T(i,i+1)U(i+1,j) \\ &= -U(i-1,j) + 2U(i,j) - U(i+1,j) \end{aligned} \tag{3.20}$$

since only three entries of row i of T are nonzero. A completely analogous argument shows that:

$$\frac{U(i-1,j) - 2U(i,j) + U(i+1,j)}{\Delta^2} = -\frac{1}{\Delta^2}U(i,j)T(i,j) \tag{3.21}$$

and so the Poisson equation may be written

$$TU + UT = b \tag{3.22}$$

The important feature of these matrices is that they are incredibly sparse and the problem is to solve for T efficiently in terms of time and storage.
Suppose we know how to factorize the solution $U = QV$, where V is a known non singular matrix and the columns of Q are eigenvectors of T. Substituting this expression for U into $TU + UT = b$ yields

$$TQV + QVT = b. \tag{3.23}$$

Now premultiply this equation by Q^{-1} to get

$$\left[Q^{-1}TQ\right]V + \left[Q^{-1}Q\right]VT = Q^{-1}b \tag{3.24}$$

or, letting D the diagonal matrix that contains the eigenvalues of T

$$DV + VT = Q^{-1}b. \tag{3.25}$$

We want to solve this equation for V, because then we can compute $U = QV$. But we have to observe that this is not a typical system. The idea to solve it is to take the transpose of the expression (3.25), we obtain:

$$V^tD + TV^t = H \tag{3.26}$$

where $H = b^t(Q^{-1})^t$ and then solving N systems for every column of V^t

$$(\lambda_i + I)V_j^t = H_j \quad j = 1, ..., N. \tag{3.27}$$

This let us with a good algorithm to solve $TU + UT = b$ for U, only computing H, V^t and V. The matrix multiplications may be a problem if we increase the number of points. We know that the cost of this operation is N^4.

3.4 Rapid method: Fourier transform solutions

For certain classes of problems, of which the Poisson problem is one example, there are rapid methods that can take advantage of some of the special properties of the underlying matrix.
Problems with regular boundaries and constant coefficient stencil can often be solved using Fourier transform or spectral techniques. The discrete inverse Fourier transform in both x and y is

$$u_{j,l} = \frac{1}{JL} \sum_{m=0}^{J-1} \sum_{n=0}^{L-1} \hat{u}_{mn} e^{-ik_m x} e^{-ik_n y} \tag{3.28}$$

where the i's in the exponentials is the imaginary number $\sqrt{-1}$ and

$$\begin{aligned} x = j\Delta x \quad & y = l\Delta y \\ k_m = \tfrac{2\pi m}{J\Delta x} \quad & k_n = \tfrac{2\pi n}{L\Delta y} \end{aligned} \tag{3.29}$$

At this point, implementing the discrete inverse Fourier transform could be done simply by $J + L$ evaluation of the summation formula (3.28). This method would have a computational complexity of $O((J + L)^2)$ multiplication operations, which is rather high for many areas of applications. There is, however, a method for the discrete Fourier transform, with a complexity of only $O((J + L)log(J + L))$ multiplication operations: the Fast Fourier Transform (FFT). To use the FFT to solve the equation (3.1), notice that because ∇^2 is a linear operator, we can find $\nabla^2 u$ by taking the Laplacian of each term in the summation,

$$\nabla^2 u_{j,l} = \frac{1}{JL} \sum_{m=0}^{J-1} \sum_{n=0}^{L-1} -(k_m^2 + k_n^2) \hat{u}_{mn} e^{-ik_m x} e^{-ik_n y} \tag{3.30}$$

but we also know that we can write the right hand side as

$$f_{jl} = \frac{1}{JL} \sum_{m=0}^{J-1} \sum_{n=0}^{L-1} \hat{f}_{mn} e^{-ik_m x} e^{-ik_n y} \tag{3.31}$$

thus term by term it must be true that

$$-(k_m^2 + k_n^2) \hat{u}_{mn} = \hat{f}_{mn}. \tag{3.32}$$

Now $\hat{f}_{mn} = \mathcal{F}[f]$ is simply the Fourier transform of the right-hand-side and is readily evaluated. Thus to solve the equation (3.1) we first find the FFT of the right-hand-side, then divide each component by $k_m^2 + k_n^2$ and then finding $u_{j,l}$ by inverse transformation

$$u_{j,l} = \mathcal{F}^{-1} \left[\frac{-\hat{f}_{mn}}{(k_m^2 + k_n^2)} \right] \tag{3.33}$$

The above procedure is valid for periodic boundary conditions. In other words, the solution satisfy

$$u_{jl} = u_{j+J,l} = u_{j,l+L}.$$

For Dirichlet boundaries where $u = 0$ we need expand the function in terms of discrete *sin* series:

$$u_{jl} = \frac{2}{J}\frac{2}{L}\sum_{m=1}^{J-1}\sum_{n=1}^{L-1}\hat{u}_{mn} sin\left(\frac{\pi jm}{J}\right) sin\left(\frac{\pi ln}{L}\right) \tag{3.35}$$

this satisfy the boundary condition that $u = 0$ at $j = 0, J$ and at $l = 0, L$. If we substitute this expansion and the analogous one for f_{jl} into equation (3.1), we find that the solution procedure is the same that for periodic boundary conditions.
These and more general boundary conditions are discussed in some detail in [41].

3.5 The fast Fourier transform (FFT)

In 1965 J.W. Cooley and J. W. Tukey published a paper [59] about a special discrete Fourier transform algorithm which they called fast Fourier transform. It was this paper which caused the widespread dissemination of the FFT [60; 61] algorithm and nowadays it is one of the truly great computational developments of this century.
The description of the FFT algorithm given in this section is based on the following proof of the *Daniel-Lanczos lemma*, which makes it possible to write a discrete Fourier transform length N (N even) as a sum of two discrete Fourier transforms of length $N/2$:

$$\begin{aligned} F_k &= \sum_{j=0}^{N-1} e^{2\pi ijk/N} f_j \\ &= \sum_{j=0}^{N/2-1} e^{2\pi i(2j)k/N} f_{2j} + \sum_{j=0}^{N/2-1} e^{2\pi i(2j+1)k/N} f_{2j+1} \\ &= \sum_{j=0}^{N/2-1} e^{2\pi ijk/(N/2)} f_{2j} + W^k \sum_{j=0}^{N/2-1} e^{2\pi ijk/(N/2)} f_{2j+1} \\ &= F_k^e + W^k F_k^o. \end{aligned} \tag{3.36}$$

F_k^e (F_k^o) denotes the k^{th} component of the Fourier transform of length $N/2$ formed from the even (odd) components of the original f_j's. The transforms F_k^e and F_k^o are periodic in k with period $N/2$, again, the required N components for F_k are obtained.
If $N/2$ is even, (3.36) can be used again on F_k^e and F_k^o. In the next step the F_k^e becomes the two Fourier transforms F_k^{ee} and F_k^{eo} of length $N/4$. For $N = 2^r$ (with $r \in N$) this can be carried out recursively r times, until identities of the form $F_k^{eooe\cdots oee} = f_n$ for any n are achieved. At this point the patterns of the e and o are changed to $e = 0$ end $o = 1$. From this point on, this operation is called a bit reversal permutation. If the resulting sequence of bits is interpreted as a binary number, then it is exactly n. It is because of the successive subdivisions of the data into even and odd values that is equivalent to the testing of the least significant bit

of the binary representation of n.
Therefore, the first part of the FFT algorithm is to interchange f_n using a bit reversal permutation. The second part has an outer loop which is executed $log_2 N$ times and calculates, in turn, transform of length $2, 4, 8, \cdots, N$. At each stage of this process, two nested inner loops range over the sub-transforms already computed and the elements of each transform implementing the Daniel-Lanczos lemma (3.36). During each stage $O(N)$ arithmetic operations are carried out. Since there are $log_2 N$ stages, the complexity of the whole FFT algorithm is of the order $O(NlogN)$.

3.6 Cyclic reduction solvers

Evidently the FFT method works only when the original PDE has constant coefficients and regular boundaries. A more general set of rapid methods, however exists for problems that are separable, in the sense of separation of variables. These methods include cyclic reduction. Numerical Recipes [41] gives a brief explanation of how these methods work which we do not repeat here. We will tell about a collection of codes called FISHPAK packages [62]. These are a collection of generalized cyclic reduction Fortran routines for solving more general Helmholtz problems, 3-D Cartesian coordinates and general 2-D separable elliptic problem, for any combination of periodic or mixed boundary conditions. These codes are extremely fast with solution time scaling like $N^2 logN$, but they were written back in the eighties and the Fortran is inscrutable and therefore hard to modify for different boundary conditions. In addition they still only work for separable problems and could not, for example solve the more general problem $\nabla \cdot k\nabla T = \rho$ for a space varying conductivity. However, the only solvers that can compete in time with these routines and handle spatially varying coefficients are the iterative multi-grid solvers.

3.7 Explicit time-stepping procedure

In previous sections we have seen how we can solve a non-linear diffusion equation as well as the Poisson equation, so we have all the elements in order to study our specific problem. The latter we remember to be:

$$\frac{\partial T}{\partial t} = \nabla^2 T + \frac{\partial \psi}{\partial y}\frac{\partial T}{\partial x} - \frac{\partial \psi}{\partial x}\frac{\partial T}{\partial y} \tag{3.37}$$

$$\nabla^2 \psi = -Ra\frac{\partial T}{\partial x}, \tag{3.38}$$

$$T(x,0) = 1; \quad T(x,1) = 0, \tag{3.39}$$

$$\frac{\partial T}{\partial x}(0,y) = \frac{\partial T}{\partial x}(1,y) = 0. \tag{3.40}$$

We first discretize equations (3.38)-(3.40) in space by using second-order centered differences at the grid point (i,j) for $i = 1, ..., N-1$ and $j = 1, ..., M-1$ ($i = 0$ or N or $j = 0$ or M represent the points on the boundary. In particular the advection

term is discretized using Arakawa scheme. The resulting equations are

$$\partial_t T_{ij} = G_1(T_{ij}, \psi_{ij}) \tag{3.41}$$
$$\nabla^2 \psi_{ij} = -RaG_2(T_{ij}) \tag{3.42}$$

where G_1 and G_2 represent finite difference approximation for all the terms except the one with time derivative in (3.42) We use second-order forward and backward differences for the boundary condition of T.
We use a second-order predictor-corrector scheme to iterate in time

$$T_{ij}^{n+1} = T_{ij}^n + \frac{\Delta t}{2}\nabla^2 T_{ij}^n + \frac{\Delta t}{2}(3J(T_{ij}^n, \psi_{ij}^n) - J(T_{ij}^{n-1}, \psi_{ij}^{n-1})). \tag{3.43}$$

More precisely, the scheme is implemented in the following way:
I. Initialization of the temperature and stream function at the time step n and also at $n-1$. We suppose that the temperature has a linear vertical distribution. The stream function is identically zero.
II. Evaluate the intermediate temperature $T^{n+\frac{1}{2}}$ by solving the implicit diffusion equation in the horizontal direction for the first half time step

$$T_{ij}^{n+1/2} = T_{ij}^n + \frac{\Delta t}{2}\nabla^2 T_{ij}^n + \frac{\Delta t}{4}(3J(T_{ij}^n, \psi_{ij}^n) - J(T_{ij}^{n-1}, \psi_{ij}^{n-1})) \tag{3.44}$$

for $i = 1, ..., N-1$ and $j = 1, ..., M-1$.
III. Implement lateral boundary conditions on $T_{ij}^{n+1/2}$.
IV. Evaluate the temperature T^{n+1} solving the implicit diffusion equation along the vertical direction for the second half time step

$$T_{ij}^{n+1} = T_{ij}^{n+1/2} + \frac{\Delta t}{2}\nabla^2 T_{ij}^{n+1/2} + \frac{\Delta t}{4}(3J(T_{ij}^n, \psi_{ij}^n) - J(T_{ij}^{n-1}, \psi_{ij}^{n-1})) \tag{3.45}$$

for $i = 1, ..., N-1$ and $j = 1, ..., M-1$.
V. Implement top and bottom boundary conditions on T_{ij}^{n+1}.
VI. Solve

$$\nabla^2 \psi_{ij}^{n+1} = -RaG_2(T_{ij}^{n+1}). \tag{3.46}$$

by the generalized cyclic reduction routine from the FISHPACK package.
VII. Implement boundary conditions on ψ_{ij}^{n+1}.
VIII. Go to the next time step.

Chapter 4

From Stationary Convection to Chaos

In this Chapter, we investigate the different behaviors of the flow patterns and heat transport in a square porous media uniformly heated from below. We start from the onset of convection to high Rayleigh number limit where the flow is chaotic. The Rayleigh number determines the nature of the flow and it characterizes the evolution of the system, from conduction at $Ra < 4\pi^2$, to vigorous convection, at higher values. Using the numerical methods described in Chapter 3 we determine the Rayleigh numbers at several transitions, which modify significantly the characteristic of the flow and the heat transport. These transitions can be of two types. The first type is a decrease in the horizontal aspect ratio of the cells. The second type is from steady to unsteady pattern. The present investigation considers value of Rayleigh number starting from 44 until 1200. It will be seen later that it is within this range that the transitions from steady to oscillatory convection and from oscillatory to chaotic convection occur.

4.1 Results of numerical simulations

The onset of convection is defined when the parallel fringe pattern of the state of pure heat conduction is slightly deformed to a wavy shape, indicating the appearance of a vertical flow component rising upward along one of the two vertical walls. At low Rayleigh number, $Ra = 44$, the convective flow begins in the most favorable mode for that value, that consists of a roll with its axis parallel to the shorter side of the box, namely the uni-cellular mode. The flow is steady. The single roll can turn clockwise or counterclockwise depending on the initial condition (we have added some noise to the initial linear temperature profile). In a single cell, the fluid is swept horizontally toward the lateral boundary. Due to buoyancy it rises and eventually impacts the upper boundary layer in the corner where the side wall meets the upper surface of the cell. In this way the fluid carries heat flux away from the hot boundary layer. In that corner the fluid is redirected horizontally, subsequently it becomes a dominant part of the fluctuation which sweeps along the upper boundary

layer, exchanging heat flux directly with the sheared, cold boundary layer. The heavier fluid goes down and crashes with the lower hot boundary layer where the colder heat flux diffuses. Notice that this scenario does not involve the central region of the cell in any way. It is remarkable that after the convection is fully developed the sense of rotation of the roll remains invariant, independent of the heating rate (until we observe transitions to new states).
Snapshots of the stream function and temperature for the solution at $Ra = 44$ are shown in Fig. 4.1.
At variance with this at high Rayleigh numbers, converged solutions display a multi-cellular convective pattern. Starting from $Ra = 350$, it exist two distinct possible modes of flow, one of which is time dependent (single cell mode), the other being steady with a three-cellular mode. The evolution of the flow is analogous to the initial onset of convection. The boundary layer becomes unstable and new upwelling sites develop. Starting from a single roll it is possible to see a continuous development of three weak circulations inside the primary convective roll. By further increasing of the heating, such circulations grow, and the flows continuously transform into a three-roll flow. This transition brings the system from a steady one-cell pattern to a steady three-cell pattern.
The aim of this investigation is the synchronization between two chaotic Hele-Shaw cells. We have to consider the synchronization between uni-cellular modes rather than multi-cellular modes. The latter being in general stationary and therefore not so interesting from the point of view of dynamical systems. By increasing the Rayleigh number, we have to be careful to keep the single cell mode of convection and this solution maybe unstable with respect to the multi-cellular modes. This task would be proven to be delicate. The pattern selection depends from the different way of heating. Indeed uni-cellular structure can be permanently maintained in the range that we have studied by a slow and controlled increase of the heating. Starting with the uni-cellular (e.g. counterclockwise) solution at $Ra = 44$ we drive the flow to remain into this mode by increasing the Rayleigh number by small increments. Hence, we force the solution into the uni-cellular mode which is unsteady for Rayleigh number larger than approximately 350. The possibility of choosing the spatial patterns born out by the experimental solutions of Caltagirone *et al*, where slight physical disturbance. A slow experimental heating produced this effect. Whereas very rapid heating introduces a multi-cellular modes (stationary). We infer that we speak about the most favorable mode, not about the most stable. Once either the steady or the oscillating state is well formed, we do not know yet if the perturbation and the change into one another is simple or not. The study of stability requires the introduction of a random perturbation in the temperature and the implementation of a numerical procedure to integrate stochastic partial differential equations. E. Helfand presented an extension of the Runge-Kutta method for stochastic ordinary differential equations [63; 64]. The implementation of this method for partial differential equations is not trivial. We shall let this task as thesis's objective.
Having chosen the time periodic mode, at $Ra = 400$ regular oscillations with non-dimensional period τ_p appear. The evolution of the solution through a single oscil-

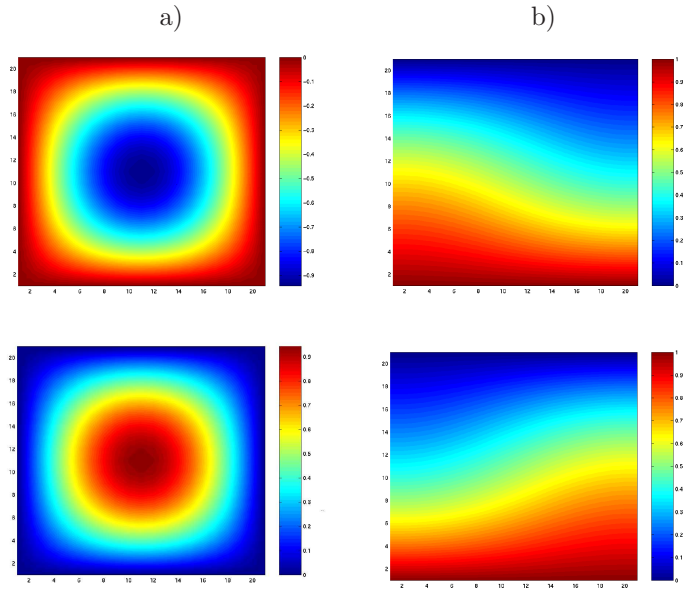

Figure 4.1: Stationary convection at Ra=44. a) The spatial pattern preferred by the flow is a uni-cellular mode (stream-function). b) The snapshots of the temperature field show clockwise and counterclockwise rotation of the roll.

lation period is illustrated in Fig. 4.2. The sequence is of five isothermal and five streamline plots evenly spaced in time ($\tau_p/4$). The numerical simulation is characterized by one prevailing frequency, $\omega_1 = 527.55 = 2\pi/\tau_p$. The power spectrum (defined as the squared modulus of the Fourier transform of the temperature taken at point $x = 10/128$,y=10/128), is particularly useful for determining the frequency of a system. The power spectrum of the Nusselt number, plotted on log linear scale, shows characteristics of single periodic regime. Figure 4.2 exhibits sharp spectral lines, standing for the the dominant frequency and its harmonics. The power spectrum of temperature is also peaked at the same frequency.

The convective system departs from this single periodic state at $Ra = 500$ when a second fundamental frequency, uncommensurable with the first, appears in the power spectrum. A close look at the Poincaré section [65] suggests a quasi-periodic dynamics. The concept of the Poincaré section follows from the observation of a system in the phase space and the consideration that the direction tangential to the flow (here flow refers to its meaning in the dynamical system theory) does not carry much interesting information. By a suitable oriented surface in the phase space, we can construct an invertible map on this surface following a trajectory of the flow. The iterates of the map are given by the points where the trajectory intersects the surface in a specified direction. In this way we reduce the phase space dimensionally by one, at the same time turning the continuous time flow in a discrete time map. The discrete time n of this map is the intersection count and is usually not simply proportional to the continuous time t of the flow. The advantage of the Poincaré section is that it permits to figure out the organization of the trajectory in the phase space. At $Ra = 520$, (Fig. 4.3), we deduce that the phase trajectory is

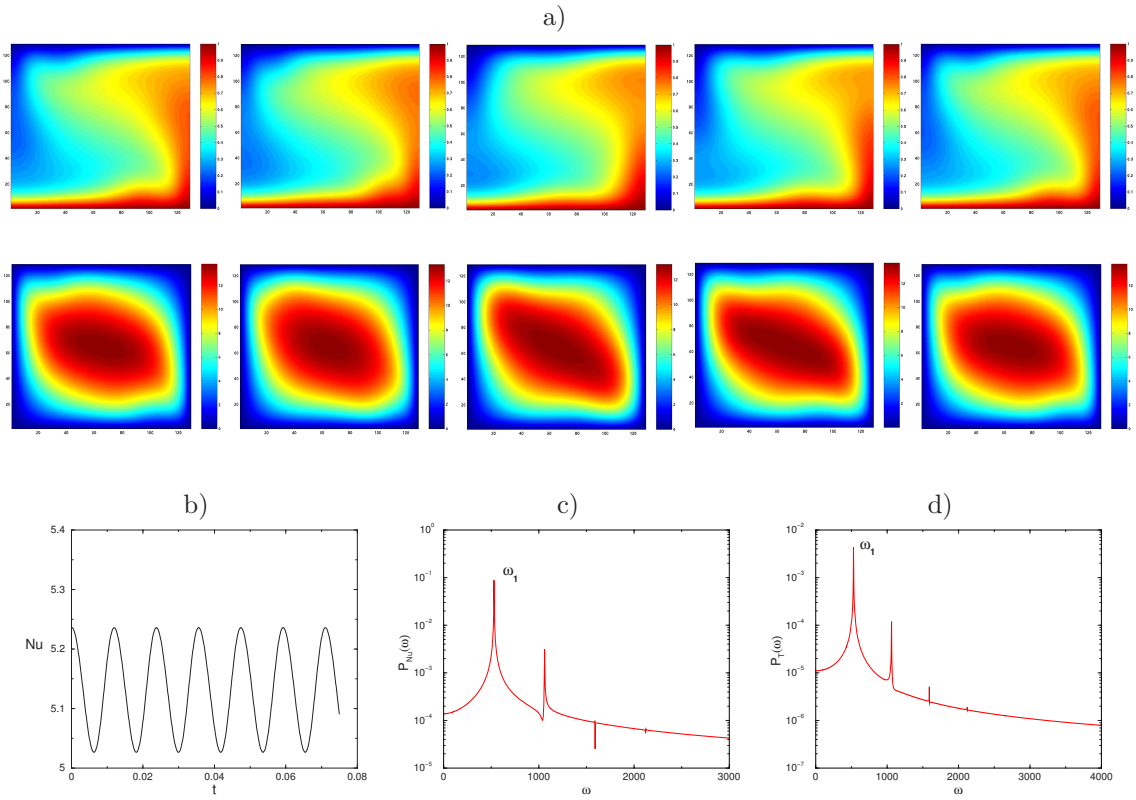

Figure 4.2: Temporal characteristics of unsteady convection at $Ra = 400$. a) Evolution of the temperature and the stream function over one oscillatory period. Time proceeds counterclockwise. The period in dimensionless units is $\tau_p = 0.01183$. b) Nusselt number as function of time. c) Power spectrum of the Nusselt number, defined as the squared modulus of the Fourier transform. Only one fundamental frequency $\omega_1 = 527.55$ and its harmonics prevail at $Ra = 400$. d) Power spectrum of temperature.

inscribed in a tore T^2, which is the attractor of a bi-periodic regime. Starting from the time series of the Nusselt number we construct the Poincaré section plotting the sequence of time intervals between successive maxima (Δt_{n+1} vs Δt_n). The frequency $\omega_2 = 655.44$ denotes the limit cycle frequency and $\omega_1 = 175.33$ is the second frequency that arises at the bifurcation (Physically it corresponds to the boundary layer oscillation instability). Figure 4.3 shows the instantaneous temperature and the stream function fields.

Many changes are observed in the spatial structure associated with the quasi-periodic state. The flow patterns are characterized by the appearance of a vertical portion of flow in the middle of the lower boundary. This portion, initially infinitesimal, grows while swept horizontally by the mean flow. By buoyancy, it rises along the side wall, moving out the lateral wall, but the rise is not uniform as in the periodic case, see Fig. 4.3. The flow breaks, creating a new particle of fluid which continues to rise upward alone. At this Rayleigh number we can observe, for the first time, the formation of thermal plumes. As an operational definition, we say that a plume is formed when an isotherm in the boundary layer is buckled. In other words, a

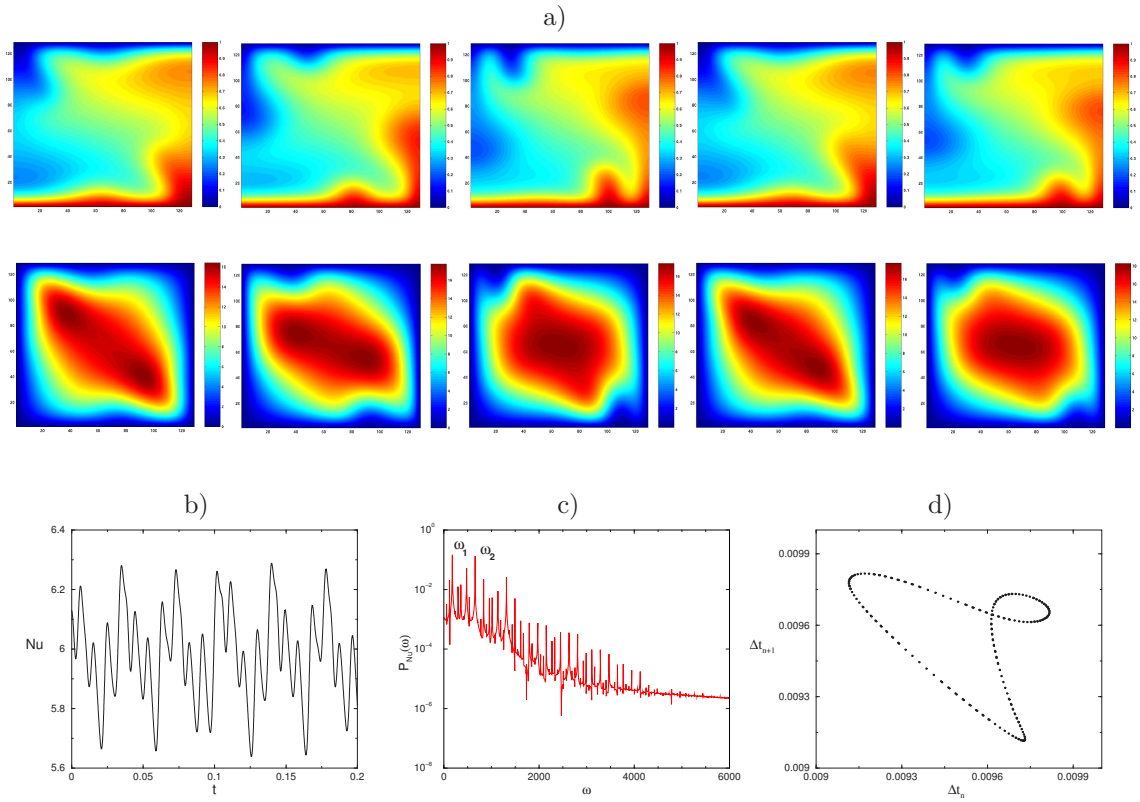

Figure 4.3: a) Snapshots of temperature and stream function for the solution at $Ra = 520$. At this value of the Rayleigh number, it appears for the first time thermal plumes. They are swept horizontally in the lower boundary layer to rise along the right lateral wall by buoyancy. b) Nusselt number as function of time. c) The spectrum of Nu shows quasi-periodic behavior: $\omega_2 = 655.44$ is the limit cycle frequency and $\omega_1 = 175.33$ is the second frequency that is born at the secondary bifurcation. d) Poincaré section plots the typical "eight" of a quasi-periodic state.

plume is formed when some portion of fluid becomes nearly vertical (away from the downstream corner). In quasi-periodic cases, no plumes are identical. The horizontal position of each plume is shifted, so with each plume formation cycle differ slightly in position relative to one another: each plume forms slightly upstream or downstream of the main position of formation. This process occurs in the following way: a fluctuation in the bottom boundary layer causes a plume to form just a little bit earlier, causing a horizontal compression of the wave train (and vertical expansion). This leads to two plumes being slightly closer to each other than they would otherwise be. These two plumes together do a more efficient job of cleaning cold fluid of the boundary layer than usual. This leads to a little longer induction time for the next plume to form, a larger interval between plumes and a slightly worse job of cleaning out the boundary layer. Thus the next plume forms a little earlier and the flow develops a phase-modulated train of disturbance. We underline that the steady solution shows the same generation of two additional cells.
Starting from $Ra = 570$ the solution returns back to a simply periodic regime. The key element is always the formation of thermal plumes, which change as Ra in-

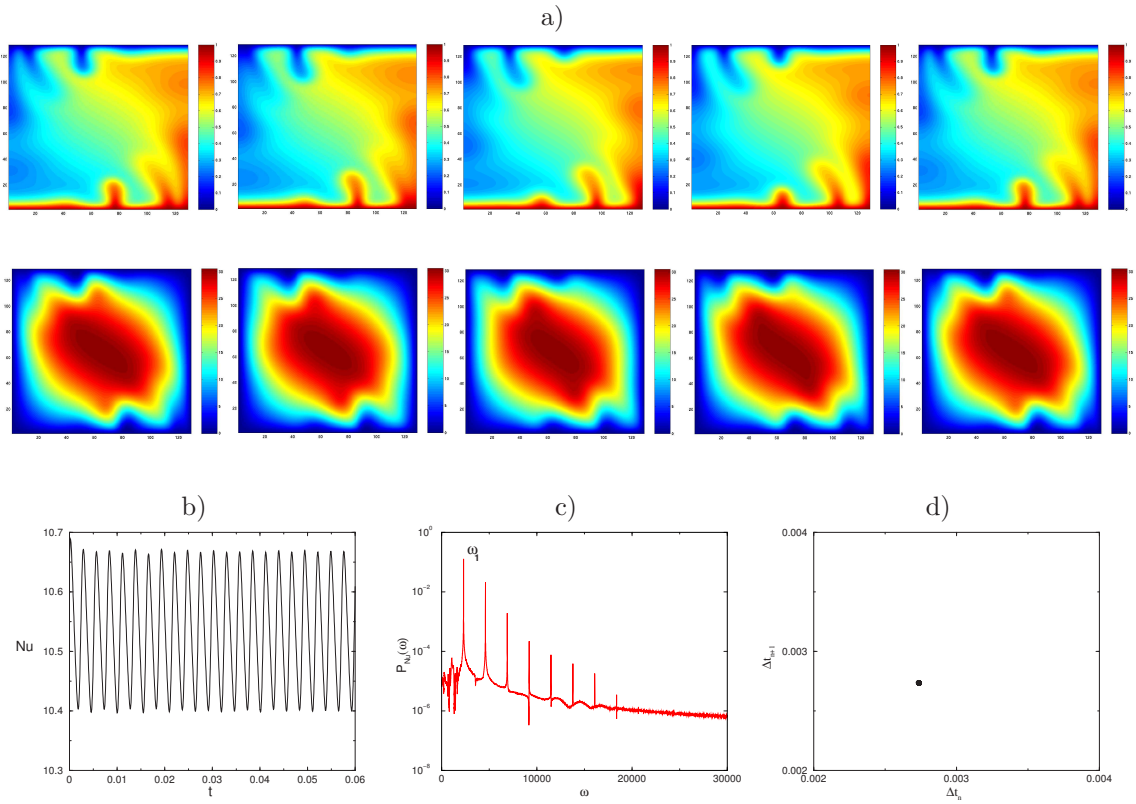

Figure 4.4: Same as figure 4.3 except that $Ra = 900$. a) Temporal evolution of the temperature and stream function over one oscillation period, $\tau_p = 0.00273$. This time sequence of the temperature shows the entire plume formation process. The overall circulation of the flow is counterclockwise. b) Nusselt number as a function of time. c) At $Ra = 900$ a single frequency, $\omega_1 = 2293.55$, and its harmonic prevail. d) Poincaré section.

creases. At $Ra = 520$ the plumes born around the middle of the bottom boundary layer. They are small and grow, more in width than in height, as they are convected across the horizontal layer. At $Ra = 900$ the plumes start closer to the left lateral boundary with greater strength. They are narrow and expand vertically.

Figure 4.4 shows, at $Ra = 900$, the evolution of the thermal plumes and stream function over one oscillatory cycle. Every plume is identical, modulo a shift in time. The period, in dimensionless units, is equal to 0.00273. The power spectrum of the Nusselt number has a single frequency, $\omega_1 = 2293.55$. The Poincaré section is very simple, it reduces to a point. The phase trajectory is a limit cycle.

Starting from $Ra = 1100$, the scenario repeats. The numerical solution shows a quasi-periodic regime.

At $Ra = 1200$ the amplitude of the variations in the heat transport reaches its maximum value and a strong broad band noise appears in the power spectrum, which is a characteristic of non-periodic motion. Exponential decay in the power spectra at high frequency is expected for bounded smooth deterministic dynamics [66; 67]. The Poincaré section shows a very large number of scattered points. The

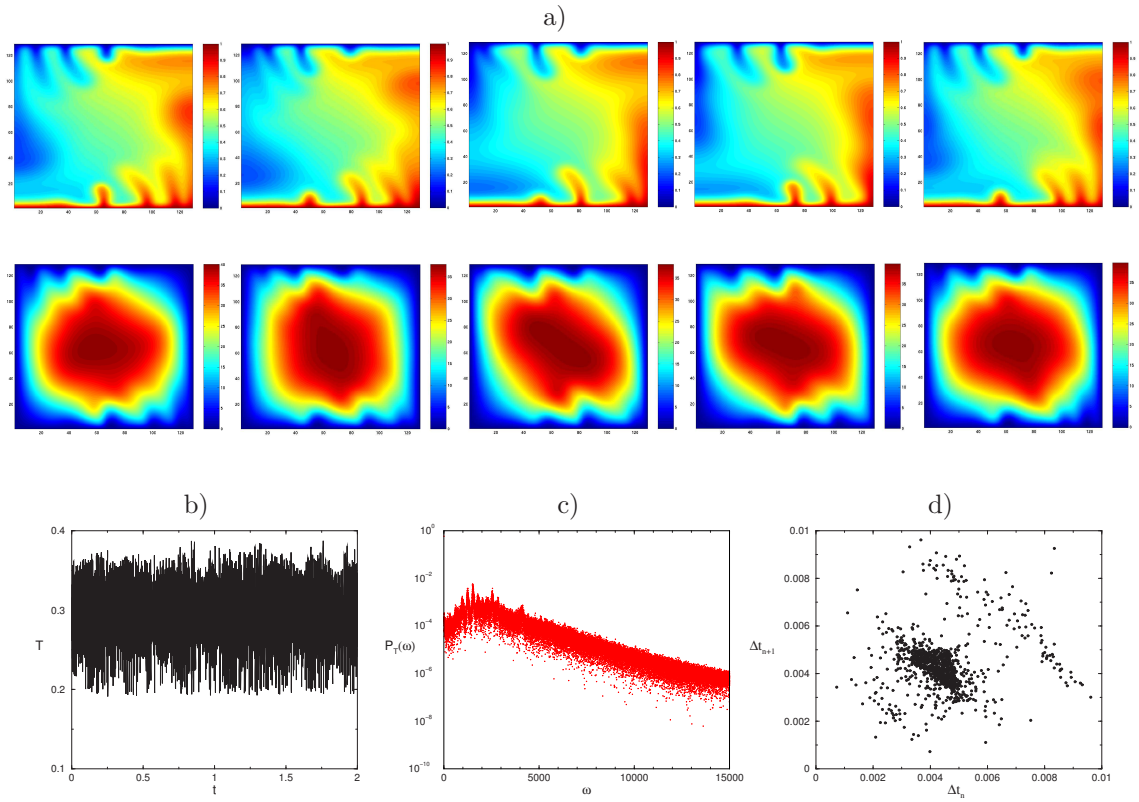

Figure 4.5: Same as figure 4.3 except that $Ra = 1200$. No single frequency prevails in the power spectrum anymore. b) Convection is in the chaotic regime. c) The power spectrum on a log linear scale illustrates the region of exponential decay. d) Poincaré section showing the scattered points.

convective regime is now chaotic. Qualitatively, however, the flow patterns appear to follow a cycle, characterized also in this case by thermal plumes. The structure is similar to those at lower Rayleigh numbers, except that the plumes are very tight and stretched. This pattern repeats itself intermittently from the left of the lower boundary without any specific regularity.

In order to gain some knowledge about the time evolution of the system one can introduce some indicators as e. g. the *autocorrelations* of a signal [68; 69]. In general, the measurement s_l of the state at time l is regarded from a probability distribution, $p(s)$, for observing different values or sequences of value. The probability distribution can be inferred from the time series. The mean of the probability distribution can be estimated by the mean of the time series

$$< s >= \frac{1}{N} \sum_{l=1}^{L} s_l \tag{4.1}$$

where $< \cdot >$ denotes the average over time and L is the total number of measurements in the time series. The variance of the probability distribution will be

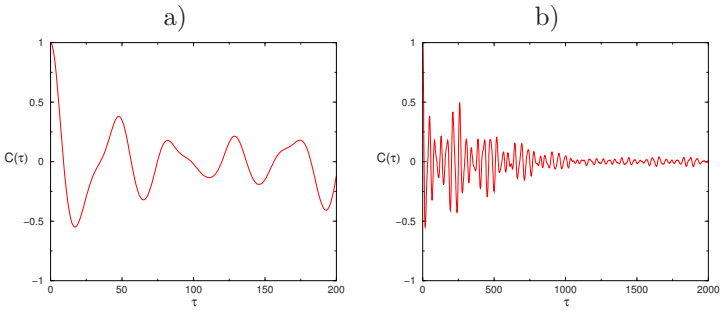

Figure 4.6: The autocorrelation function of the temperature signal at point $x = 10/128$; $y = 10/128$. a) is close up of b), τ is the lag time ($\tau = \nu\Delta t$).

estimated by the variance of the time series

$$\sigma^2 = \frac{1}{N-1}\sum_{l=1}^{L} s_l(s_l - < s >)^2. \tag{4.2}$$

The autocorrelation at lag time ν is given by

$$c_\nu = \frac{< (s_l - < s >)(s_{l-\nu} - < s >) >}{\sigma^2}. \tag{4.3}$$

If we plot the values s_l versus the corresponding values at fixed ν, the autocorrelation c_ν quantifies how these points are related. If they are not correlated then $c_\nu = 0$. If the signal is observed over a continuous time, one can introduce *autocorrelation function* $C(\tau)$ and the correlation of equation (4.3) are estimates of $C(\tau = \nu\Delta t)$. Obviously, $C_0 = 1$.
Autocorrelation of signals from chaotic systems decay exponentially with increasing lag time [65]. Our simulations indicate, indeed, that the correlation functions of the temperature, decay exponentially (at least for the envelope of the function). The spatial correlation function of the temperature has the same behavior. Figure 4.7 shows the spatial correlation curves between points at three different heights ($y = 1/4$, $y = 1/2$ and $y = 3/4$).

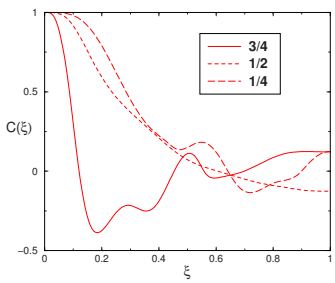

Figure 4.7: The spatial correlation function of the temperature for $x \in [0, 1]$, at $y = 1/4$, $y = 1/2$ and $y = 3/4$.

Chapter 5

Synchronization

In the previous chapter we have shown that by heating uniformly from below an Hele-Shaw cell a large number of different dynamical regimes may appear: stationary convection, oscillatory convection, thermal plumes and turbulent flow. This richness of different behaviors, in a rather simple geometry, seems a good candidate in order to study possible synchronization mechanisms between two identical cells. We give particular emphasis to the synchronization of chaotic dynamics. Indeed, this problem has attracted much attention during the last few years because of its role in the understanding of coupled nonlinear systems.
In this context of different behaviors many different synchronization states have been identified: complete synchronization, phase synchronization, general synchronization, etc... [23].
Here we have chosen to characterize the first discovered and certainly the simplest form of synchronization i.e. the complete synchronization.
Different coupling schemes have been proposed in order to achieve synchronization. A widely used coupling, and controlling, technique is the so called "pinning" technique [70; 71; 72; 73], which connects pair of points of the two systems.

5.1 Complete synchronization

For chaotic dynamics, synchronization influences not only the mean frequencies but also the chaotic amplitudes. As a result, the signals coincide (or nearly coincide).
Let us consider the temporal evolution of two identical chaotic systems:

$$\begin{aligned} \dot{\mathbf{x}} &= \mathbf{f}(\mathbf{x}), \\ \dot{\mathbf{y}} &= \mathbf{f}(\mathbf{y}), \end{aligned} \tag{5.1}$$

where $\mathbf{x}$ and $\mathbf{y}$ represent the N-dimensional state vectors of the systems, while $\mathbf{f}$ is a vector field $\mathbf{f} : R^n \rightarrow R^n$. As the dynamics of each variable is chaotic, in the case of non interacting systems one sees two independent random-like processes without any mutual correlation. Now let us introduce an interaction between the two systems. Obviously, there is not a unique way to couple. However, we are

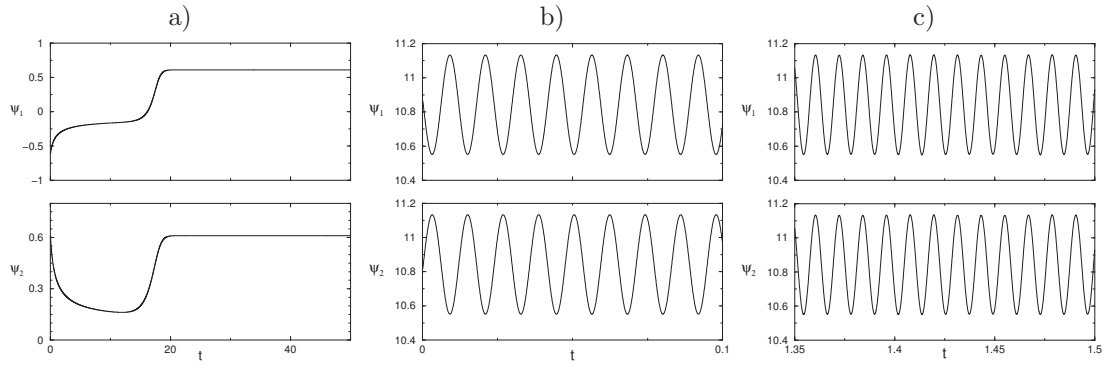

Figure 5.1: Time series of ψ_1 and ψ_2 at the point $x = 1/3$; $y = 1/3$. a) Complete synchronization for steady convection at $Ra = 44$. Complete synchronization for periodic convection at $Ra = 400$. b) At the beginning the time series are out of phase. c) Under the presence of the coupling the periodic oscillations come in phase.

looking for a contractive coupling that tends to make the differences $|\mathbf{x} - \mathbf{y}|$ smaller and does not affect the symmetric synchronous state $\mathbf{x} = \mathbf{y}$. Therefore, we demand that the coupling force were proportional to the differences of the state of the two systems and vanishes for coinciding state.
A bidirectional coupling scheme is obtained by introducing the following additional dissipation term:

$$\begin{aligned} \dot{\mathbf{x}} &= \mathbf{f}(\mathbf{x}) + \mathbf{C} \cdot (\mathbf{y} - \mathbf{x}) \\ \dot{\mathbf{y}} &= \mathbf{f}(\mathbf{y}) + \mathbf{C} \cdot (\mathbf{x} - \mathbf{y}) \end{aligned} \tag{5.2}$$

where $\mathbf{C}$ is a $n \times n$ matrix, whose coefficients rule the dissipative coupling. If there is no coupling the two systems are completely independent and uncorrelated; with small coupling the trajectory of the signals will move closer due to the attraction between the two states. If the coupling is strong enough the attraction wins and eventually it can lead to a complete synchronized state.

5.1.1 All internal points are connectors

Starting from two identical Hele-Shaw cells, we introduce a thermal bidirectional coupling between *all* the internal points. Adding the dissipation term to the equations (3.42) and (3.43), the systems are governed now by

$$\text{I} \quad \begin{cases} \frac{\partial T^{(1)}}{\partial t} = \nabla^2 T^{(1)} + J(T^{(1)}, \psi^{(1)}) + \epsilon(T^{(2)} - T^{(1)}) \\ \\ \nabla^2 \psi^{(1)} = -RaG_2(T^{(1)}) \end{cases}$$

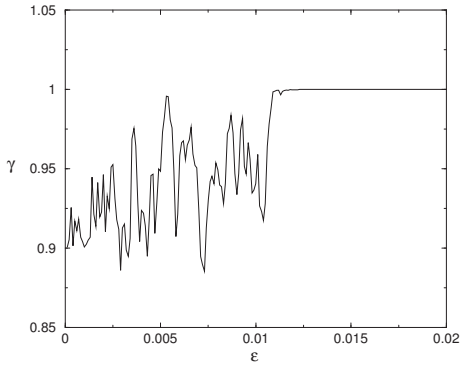

Figure 5.2: Pearson's coefficient (see text for definition) vs the thermal coupling ϵ.

$$\text{II} \quad \begin{cases} \frac{T^{(2)}}{\partial t} = \nabla^2 T^{(2)} + J(T^{(2)}, \psi^{(2)}) + \epsilon(T^{(1)} - T^{(2)}) \\ \\ \nabla^2 \psi^{(2)} = -RaG_2(T^{(2)}) \end{cases}$$

where the indexes 1 and 2 refer to the two systems, ϵ is the thermal coupling and is applied in all the interior points $(i, j = 1, ..., N-1)$.
Before presenting the results for the synchronization of chaotic systems, we want to briefly discuss the cases of steady and periodic convection.
At $Ra = 44$, two systems with a single convective cell, the first system with clockwise rotation, the second one with counterclockwise rotation are prepared. By setting the thermal coupling ϵ, which value lies in the interval $[0.35, 1]$, synchronization between the two cells is achieved. The cell of the first system begins to turn counterclockwise. The figure 5.1*a* shows complete coincidence of the two systems after some transient, for the coupling $\epsilon = 0.5$.
For the periodic case, $Ra = 400$, the two cells are prepared with counterclockwise rotation but they are initially out of phase, see Fig. 5.1b. This can be done by taking as initial conditions for the second system the final state of the first after a time of exactly half period. By applying a thermal coupling $\epsilon = 0.05$ after 1000 iterations, the two periodic states return in phase, see figure 5.1*c*. We underline that this is the simplest case. We pass through two different states of synchronization: from synchronization in anti-phase to synchronization in phase.

Let us now come to discuss the case of chaotic dynamics at $Ra = 1200$. In this case, the correlation function gains much interest because it is one central measure for quantifying synchrony. Recent papers illustrate the power of the correlation in measuring the synchrony [74; 75; 76]. The most common way to quantify the degree of synchronization between two variables is by monitoring the Pearson's coefficient γ, or zero-lag cross-correlation

$$\gamma = \frac{< (T_1 - < T_1 >)(T_2 - < T_2 >) >}{\sigma_1 \sigma_2} \tag{5.4}$$

where we recall that $<>$ and σ^2 denote a full space-time average and variance, respectively, and T_1 and T_2 are the temperature field of the two systems. Precisely,

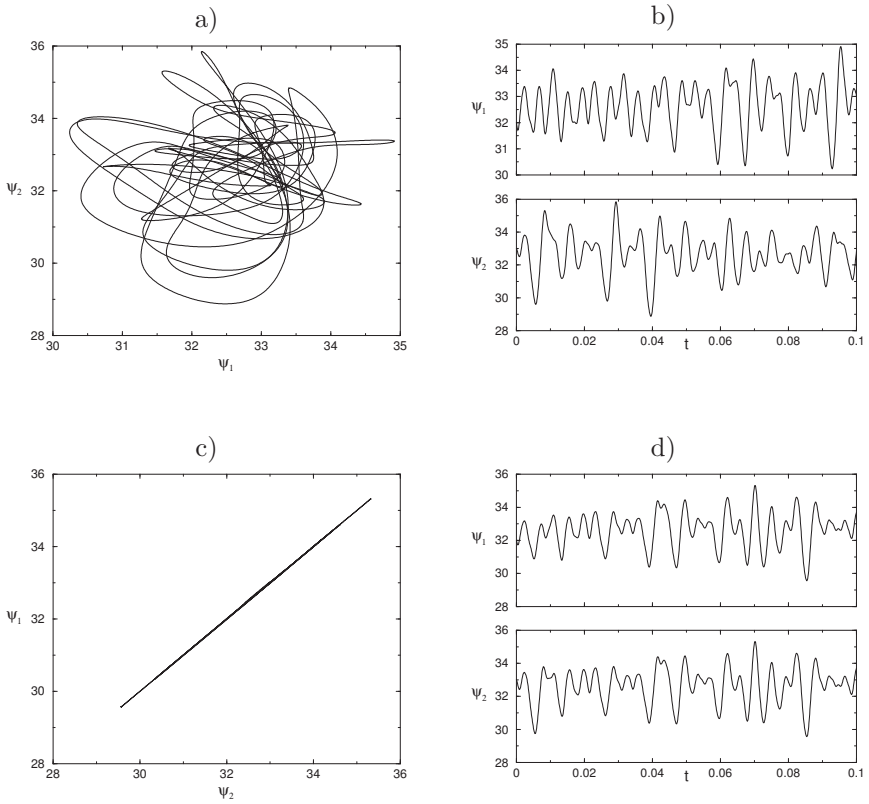

Figure 5.3: a) Uncoupled Hele-Shaw cells, ψ_1 vs ψ_2 ($\epsilon = 0$, $x = 1/3$; $y = 1/3$). b) Time series of the stream function below the synchronization threshold. c) and d) Complete synchronization in coupled Hele-Shaw cells ($\epsilon = 0.05$). The states of the systems are identical.

when $\gamma = 0$ the two fields are linearly uncorrelated; $\gamma = 1$ marks complete correlation and $\gamma = -1$ indicates that the fields are negatively correlated. Figure 5.2 reports the Pearson's coefficient as function of the thermal coupling ϵ. The results indicate that for value of the coupling smaller than 0.02 the Pearson's coefficient is almost one. But, as we will see later, this not means the appearance of a complete synchronization state for these low values of the coupling.

The cells have been prepared both with counterclockwise rotation but different initial conditions. The proper way to do this is analog to what we did for the periodic case. In order to see the differences between the systems we plot the variables of system I vs the variables of system II, (a Lissajous-type plot) as in Fig. 5.3a. Of course, the time series give us the same information as in Fig. 5.3b.

We connect the two systems with couplings $\epsilon = 0.5, 0.05, 0.02, 0.01$ at the dimensionless time $t = 0.01$. Once we get synchronization, the states of the systems are identical, as it can be easy seen on the plot ψ_1 vs. ψ_2, Fig. 5.3c. The trajectory lies on the diagonal $\psi_1 = \psi_2$. However, it is important to note that the coupling does not destroy the chaotic dynamics, but the oscillations are nearly identical, as shown in figure 5.3d.

In order to verify the complete synchronization we have defined the synchronization

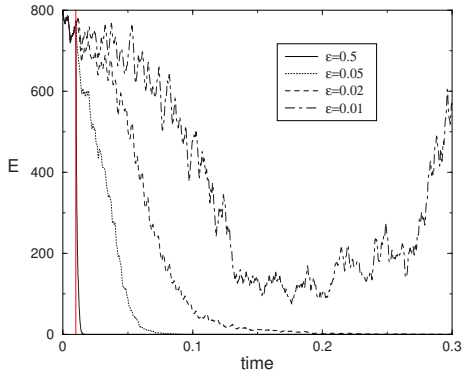

Figure 5.4: Synchronization error E (see text for definition), for several values of the coupling strength. The convergence rate is proportional to ϵ. For $\epsilon = 0.01$ synchronization is not achieved.

error as:

$$E = \sum_r |T_1(r) - T_2(r)| \tag{5.5}$$

where r stands for all the interior points. Another important parameter for characterizing the synchronization is the time that we have to wait in order to obtain the perfect coincidence of the trajectories of the two systems. The error has a practical importance, in fact we decide to stop the program when the error is less than 10^{-6}, a value for which we are sure to have reach a synchronized state. In figure 5.4 the error is plotted for different values of the coupling. Obviously, the rate of convergence to the synchronized state is faster for stronger couplings. For weaker couplings the transient times increase. There is a critical value of ϵ below which synchronization is no longer obtained. The space-time plots of the cells taken at height $h = 10/128$ (from the bottom wall) are shown in Fig. 5.5, showing the dynamics of the plumes drifting to the right wall after being created. At time $t = 0.01$ the coupling is switched on with $\epsilon = 0.5$. Immediately after the coupling is set, the states are still different but come close one to another and they converge slowly towards the synchronized state.

5.1.2 Coupling through the lateral walls (only)

Until now, we have shown theoretically that synchronization between two Hele-Shaw cells is possible for a sufficiently large coupling. We want to consider also the feasibility from the experimental point of view. This is not an easy task. An obvious limitation is how to implement the coupling between the two convective cells without perturbing too much the system. The coupling technique used thus far consisted in connecting the whole spatial domain. This is not clear yet how to realize such a connection between all the internal points of the systems. This may also be impractical in experiments. On the other hand, because of the smallness of the spatial correlation length (see figure 4.7), it seems (at least intuitively) that we need to put several internal connectors between the two systems. This number of

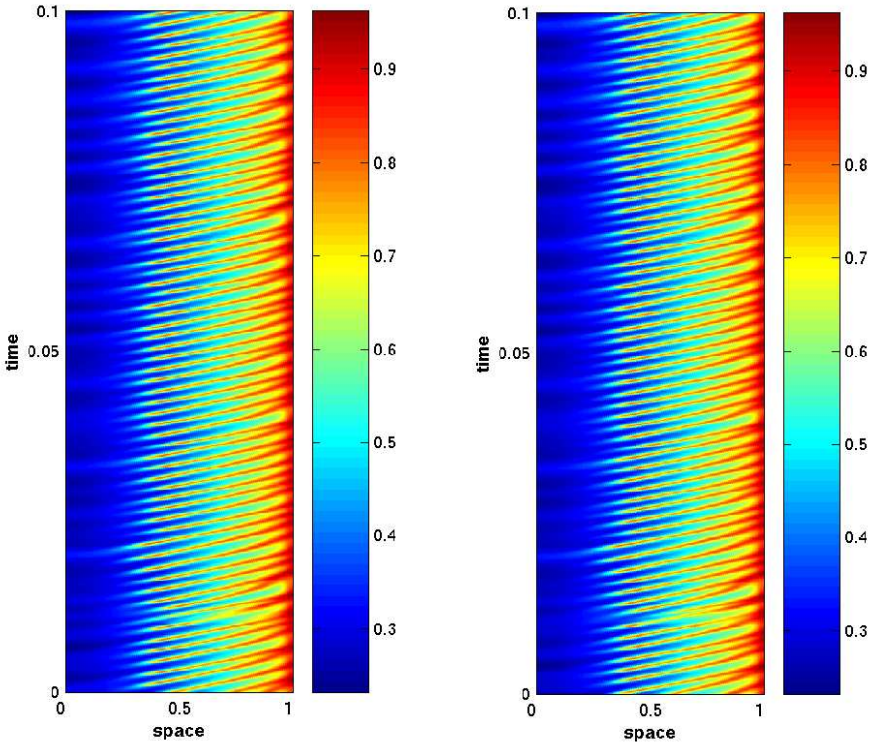

Figure 5.5: Space-time plots of the two convective cells at $h = 10/128$. At time $t = 0.01$ the coupling ($\epsilon = 0.5$) is switched on.

connectors must be finite and as small as possible. The reason for which we do not couple in the whole spatial domain is that the uncoupled areas receive correlation with the coupled areas that are in their neighborhood. They receive the information about the dynamics through the internal spatial diffusion inside the system. In addition we should mention also that the experimental measuring devices have a finite time resolution and measure local spatial information of some observable.
Let us now give a brief account of the experiment. It has been thought to work by using the Peltier effect in order to put or extract heat from the system. In 1934 J. Peltier discovered that the passage of an electric current through the junction of two dissimilar conductors can either cool or heat this junction, depending on the direction of the current. Heat generation or absorption rates are proportional to the magnitude of the current and also the temperature of the junction. Let us now return to our numerical simulation, the cells are prepared with different initial conditions. Both cells have Peltier devices on each lateral boundary. The position of them is the same for the two cells. The temperature of the fluid around each Peltier device is constantly measured. A same fluid's parcel has a different temperature in the two cells. The Peltier device in contact with warmer fluid will extract heat and locally cools the surrounding fluid, the corresponding device in the other cell will inject heat. This will last until the temperature measured in both systems are equilibrated.
In order to test the feasibility of this experimental setup, we are using controllers

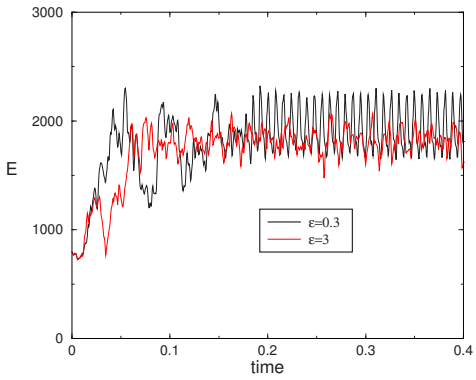

Figure 5.6: Synchronization error using a weak and a very strong coupling connecting only the points located at the lateral boundaries. Synchronization is not achieved in these cases.

only belonging to the lateral walls i.e. 256 mesh points. With this particular choice the systems are governed always by the same equations (5.3), where the term $\epsilon(T_{i,j}^{2,1} - T_{i,j}^{1,2})$ appears when $i = 1, ..., N-1$, but only $j = 1$ and $j = N-1$. An inspection of the synchronization errors suggest that this type of connection is not strong enough to achieve synchronization. From Fig. 5.6, we observe that the synchronization error increases in time by using a very strong coupling, $\epsilon = 3$.

5.1.3 Finite number of internal points are used as connectors

The failed attemp of synchronization through the lateral walls brings us to investigate the minimal number of "internal" points necessary in order to obtain synchronization. In experiment one will try to use as few controllers as possible.

The simplest way to start investigating the minimal number of controllers is to put the connectors every two grid points and, in case of success, following the reduction of connectors in this way. This strategy permits to get synchronization, but we observe a change in the organization of the pattern structure, see figure 5.7. For a connector every two grid points, the flow passes from a single roll cell (chaotic) to a three-cellular convection mode (stationary). The convergence to the synchronization state is not fast. Here the synchronization drastically affect the final dynamical state of the system i.e. we have chaos suppression. Presumably, the basin of attraction of the single chaotic cell is quite narrow and a sparse and strong coupling will lead to fall in the three-cellular steady solution. The reason is that this solution is selected when strong perturbations are applied to the single chaotic cell. In order to avoid to destroy the single cell solution, we have to increase very slowly the coupling from zero to its nominal value. Unfortunately, all attempts to keep the single mode with less connectors have failed so far. Even worse, is the case of a connector every four grid points, in that case the synchronization is no longer achieved and the solution single mode is destroyed into a two-cellular solution that is still chaotic.

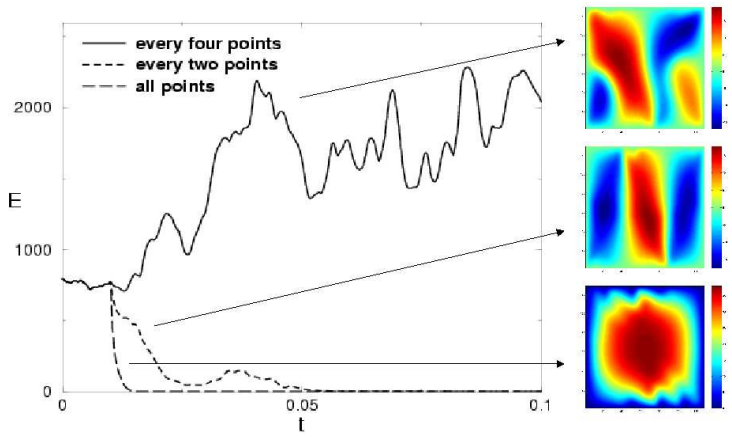

Figure 5.7: The synchronization error obtained by connecting all the points, every two points and every four points. The coupling parameter, $\epsilon = 0.5$, is set at $t = 0.01$. For a loose connection (every two points) a new three-cellular stationary structure appears. For a connector every four points, synchronization is not achieved.

Conclusions, discussions and further works

In this work we have studied possible ways to synchronize two Hele-Shaw cells. This objective has required first to study the dynamics of a single Hele-Shaw cell. The Hele-Shaw cell has been defined in the first chapter and it is interesting for us as a simple system possessing a boundary layer instability at reasonably large Rayleigh number. There is no analytical tools available for solving nonlinear complicated PDE. Therefore, in chapter 2 and 3, we have recalled the numerical techniques that permit to calculate the time evolution of the flow inside the convective cell. In Chapter 4, we have displayed the results of the integration of a Hele-Shaw cell for different values of the Rayleigh number. By increasing this parameter, we pass from stationary to oscillatory and chaotic convection with also formation of thermal plumes. Thermal plumes are generated in the lower unstable boundary layer.

One thing that comes clear from reading Chapter 4, is the dynamical richness of the Hele-Shaw cell. For a fixed value of the Rayleigh number, the system exhibits multistability. Several solutions are possible depending on the initial conditions. The question of stability of these multiple solutions has not been considered in this thesis and is the first objective that we plan to pursue in the future. A "phase" diagram is the goal, i.e. for a fixed value of the Rayleigh number what are the solutions stable and unstable and for each of the stable solution what is the basin of attraction of the solution. This study will certainly been time consuming but some tools can help in this task as e.g. Auto2000 [77] (a bifurcation analysis package for ODE). In the same objective, we plan to perturb the solutions with different type of noise (starting from white Gaussian noise and then more complicated "colored" noise) in order to study how robust the solutions are. In the process of drawing the "phase" diagram of the Hele-Shaw cell, it may be useful to reduce the PDE to a large set of ODE as it has been done by Dauby [78] in the case of Benard-Marangoni convection in small containers.

We thought interesting to use the synchronization techniques in this realistic PDE system. In Chapter 5, we have presented some preliminary results on the synchronization of two Hele-Shaw cells. Synchronization is possible if the cells are coupled with all the internal points and a sufficient strong coupling. These requirements are quite demanding and in view of future experimental realization not very encouraging. Let us recall that synchronization through the lateral walls failed as

well as for a loose coupling when only every 4 grid points were connected in space, as it is detailed in the end of Chapter 5. These first numerical results are not very promising for experimental realization but we are planning to use a new technique for control based on the Floquet theory [79] that has permitted giant improvement in the control of spatial structures in semiconductor devices. Also in the connection with experiments, we want to use finite area of coupling rather than the less realistic "pinning" control used in Chapter 5, this will be based on some recent work of Junge and Parlitz [72].

As it is often the case, this investigation has opened more doors than has given definitive answers.

Bibliography

[1] P. Bergé and M. Dubois. Rayleigh-Bénard Convection. *Contemp. Phys.*, 25:535–582, 1984.

[2] H. Bénard. Les tourbillons cellulaires dans une nappe liquide. *Rev. Gen. Sci. Puers Appl.*, 11:1261–1271, 1900.

[3] Rayleigh, Lord. On convection currents in a horizontal layer of fluid when the higher temperature is on the under side. *Philos. Mag.*, 32:529–546, 1916.

[4] S.H. Davis. Convection in a box: linear theory. *J. Fluid Mech.*, 30:465–478, 1967.

[5] S.H. Davis. Convection in a box: on the dependence of preferred wave-number upon the Rayleigh number at finite amplitude. *J. Fluid Mech.*, 32:619–624, 1968.

[6] E.L. Koschmieder. On convection on a uniformly heated plane. *Beitr. Phys. Atmos.*, 39:1–11, 1966.

[7] E.L. Koschmieder. On convection on a non-uniformly heated plane. *Phys. Rev. Lett.*, 39:208–216, 1966.

[8] J.N. Koster and U. Müller. Convection in boxes: an experimental investigation in vertical cylinder and annuli. *J. Fluid Mech.*, 71:231–240, 1975.

[9] T. Ondarcuhu, J. Millán-Rodriguez, H. Mancini, A. Garciamartín and C. Perez-Garcia. Bénard-Marangoni convective patterns in small cylindrical layers. *Phys. Rev. E*, 48:1051, 1993.

[10] M.L. Ramón, D. Maza and H. Mancini. Patterns in a small aspect ratio Bénard-Marangoni convection. *Phys. Rev. E*, 60:4193–4198, 1999.

[11] J.N. Koster and U. Müller. Time-dependent free convection in vertical slots. *Phys. Rev. Lett.*, 47:1599–1602, 1981.

[12] J. Bear. *Dynamics of Fluid in Porous Media*. New York, 1972.

[13] D.A. Nield and A. Bejan. *Convection in Porous Media*. New York, 1999.

[14] C.W. Horton and F.T. Rogers. . *J. Appl. Phys.*, 16:367, 1945.

[15] E.R. Lapwood. Convection of a fluid in a porous medium. *Proc. Camb. Phil Soc.*, 44:508–521, 1948.

[16] J.P. Caltagirone, M. Cloupeau and M. Combarnous. Convection naturelle fluctuante dans une couche poreuse horizontale. *Acad. Sci. Paris*, 273:833–836, 1971.

[17] R.N. Horne and M.J. O'Sullivan. Oscillatory convection in porous medium heated from below. *J. Fluid Mech.*, 66:339–352, 1974.

[18] A.S.M. Cherkaoui and W.S.D. Wilcock. Characteristics of high Rayleigh number two-dimensional convection in an open-top porous layer heated from below . *J. Fluid Mech.*, 394:241–260, 1999.

[19] M. P. Arroyo and J. M. Savirón. Rayleigh-Bénard convection in a small box: spatial features and thermal dependence of the velocity field. *J. Fluid Mech.*, 235:325–348, 1992.

[20] A. Pikovsky, M. Rosenblum and J. Kurths. *Synchronization, A Universal Concept in Nonlinear Sciences*. Cambridge University Press, UK, 2001.

[21] C. Huygens. *Horologium Oscilatorium*. Paris, France, 1673.

[22] L.M. Pecora and T.L. Carroll. Synchronization in chaotic systems. *Phys. Rev. Lett.*, 64:821–824, 1990.

[23] S. Boccaletti, J. Kurts, G. Osipov, D.L. Valladares and C.S. Zhou. The synchronization of chaotic systems. *Phys. Rep.*, 366:1–101, 2002.

[24] L. Kocarev and U. Parlitz. General approach for chaotic synchronization with applications to communication. *Phys. Rev. Lett.*, 74:5028–5031, 1995.

[25] U. Parlitz, L. Kocarev, T. Stojanovski and H. Preckel. Encoding messages using chaotic synchronization. *Phys. Rev. E*, 53:4351–4361, 1996.

[26] S.H. Strogatz. *Nonlinear Dynamics and Chaos*. Addison–Wesley, USA, 1994.

[27] D. Pnueli and C. Gutfinger. *Fluid Mechanics*. Cambridge University Press, 1992.

[28] R. Peyret. *Spectral methods for incompressible viscous flow*. Springer, New York, 2002.

[29] W.J. Minkowycz, E.M. Sparrow, G.E. Schneider and R.H. Pletcher. *Handbook of numerical heat transfer*. Wiley,New York, 1988.

[30] J.D. Lambert. *Numerical methods for ordinary differential systems: the initial value problem*. Wiley & Sons, London, 1991.

[31] R.D. Cook. *Concept and applications of finite element analysis*. Wiley & Sons, New York, 1981.

[32] A.J. Davies. *The finite element method: a first approach*. Clarendon Press, Oxford, 1980.

[33] L.N. Trefthen. *Spectral methods in MATLAB*. PA: Society for Industial and Applied Mathematics, Philadelphia, 2000.

[34] B. Mercier. *An introduction to numerical analysis of spectral methods*. Springer, Berlin, 1989.

[35] D. Gottlieb and S.A. Orszag. *Numerical analysis of spectral methods: theory and application*. Society for Industial and Applied Mathematics, Philadelphia, 1993.

[36] C. Jordan. *Calculus of finite differences*. Chelsea publishing company, New York, 1965.

[37] L.M. Milne-Thomson. *The calculus of finite differences*. Macmillan and Co., New York, 1965.

[38] G.D. Smith. *Numerical solution of partial differential equations: finite difference methods*. Oxford University Press, New York, 1999.

[39] R. Courant. *Differential and integral calculus*. Interscience, 1970.

[40] E. Landau. *Differential and integral calculus*. Chelsea, New York, 1965.

[41] W.H. Press. *Numerical recipes in FORTRAN: the art of scientific computing*. Cambridge University Press, Cambridge, 1992.

[42] M. Spiegelman. *Myths & Methods in Modeling*. www.ldeo.columbia.edu/∼mspieg, 2000.

[43] W. E and J. Liu. *Vorticity boundary condition and related isuue for finite difference schemes*. www.math.umd.edu/∼jliu/research, 2000.

[44] W. E and J. Liu. *Essentially compact schemes for unsteady viscous incompressible flows*. www.math.umd.edu/∼jliu/research, 2000.

[45] S. Weart. *Arakawa's Computation Trick*. www.aip.org/history/climate, 2001.

[46] J.M. Beckers. *Méthodes numeriques appliquées à l'environnement*. http://modb.oce.ulg.ac.be, 2002.

[47] J.M. Beckers. *Mécanique des fluides non-homogènes*. http://modb.oce.ulg.ac.be, 2000.

[48] G.H. Golub and C.G. Van Loan. *Matrix Computations*. Johns Hopkins University Press, Baltimore, 1983.

[49] C.T. Kelley. *Iterative Methods for Linear and Nonlinear equations*. SIAM, Philadelphia, 1995.

[50] C.W. Ueberhuber. *Numerical Computation 2, Methods, Software and Analysis*. Springer, Berlin, 1997.

[51] D.F. Elliot and K.R. Rao. *Fast Transform: Algorithms, Analyses, Applications*. Academic Press, New York, 1982.

[52] H.J. Nussbaumer. *Fast Fourier Transform and Convolution Algorithms*. Springer-Verlag, Berlin, 1981.

[53] C. Van Loan. *Computational Framework for the Fast Fourier Transform*. SIAM Press, Philadelphia, 1992.

[54] J.M. Lopez and J. Shen. An efficient spectral-projection method for the Navier-Stokes equations in cylindrical geometries. *J. Comput. Phys.*, 139:308–326, 1998.

[55] G.L. Brown and J.M. Lopez. Axisymmetric vortex breakdown, Part 2. Physical mechanisms. *J. Fluid Mech.*, 221:553–576, 1990.

[56] J.M. Lopez. Axisymmetric vortex breakdown, Part 1. Confined swirling flow. *J. Fluid Mech.*, 221:533–552, 1990.

[57] J.M. Lopez and A.D. Perry. Axisymmetric vortex breakdown, Part 3. Onset of periodic flow and chaotic advection. *J. Fluid Mech.*, 234:449–471, 1992.

[58] R.E. Lynch, J.R. Rice and D.H. Thomas. Direct solution of partial differential equations by tensor product methods. *Numer. Math.*, 6:185–199, 1964.

[59] J.W. Cooley and J.W. Tukey. An algorithm for the machine calculation of complex Fourier series . *Math. Comp.*, 19:297–301, 1965.

[60] E.O. Brigham. *The fast Fourier transform*. Englewood Cliffs: Prentice-Hall, 1974.

[61] E.O. Brigham. *The fast Fourier transform and its application*. Englewood Cliffs: Prentice-Hall, 1988.

[62] P.N. Swarztrauber and R.A. Sweet. Efficient FORTRAN subprograms for the solution of elliptic partial differential equations. *ACM Trans. Math. Soft.*, 5:352, 1979.

[63] E. Helfand. Numerical integration of Stochastic Differential Equations . *The Bell System Technical Journal*, 58:2289–2299, 1979.

[64] E. Helfand. Numerical integration of Stochastic Differential Equations-II . *The Bell System Technical Journal*, 60:1927–1940, 1981.

[65] P. Bergé, Y. Pomeau and C. Vidal. *L'ordre dans le chaos. Vers une approche déterministe de la turbulence*. Hermann, Paris, 1984.

[66] M.R. Paul, M.C. Cross, P.F. Fischer and H.S. Greenside. Power law behavior of power spectra in low Prandtl number Rayleigh Bénard convection. *Phys. Rev. Lett.*, 87:154501/1–4, 2001.

[67] U. Frisch and R. Morf. Intermittency in nonlinear dynamics and singularities at complex times. *Phys. Rev. A*, 23:2673–2705, 1981.

[68] H. Kantz and T. Schreiber. *Nonlinear time series analysis*. Cambridge University Press, 1997.

[69] R. Hegger, H. Kantz and T. Schreiber. *Practical implementation of nonlinear time series methods: The TISEAN package*. www.mpipks-dresden.mpg.de, 1998.

[70] G. Hu and Z. Qu. Controlling spatiotemporal chaos in coupled map lattice systems . *Phys. Rev. Lett.*, 72:68–71, 1994.

[71] R.O. Grigoriev, M.C. Cross and H.G. Schuster. Pinning control of spatiotemporal chaos . *Phys. Rev. Lett.*, 79:2795–2798, 1997.

[72] L. Junge and U. Parlitz. Synchronization and control of coupled Ginzburg-Landau equations using local coupling. *Phys. Rev. E*, 61:3736–3742, 1999.

[73] S. Boccaletti, J. Bragard and F.T. Arecchi. Controlling and synchronizing space time chaos. *Phys. Rev. E*, 59:6574–6578, 1999.

[74] O.N. Bjornsatd, R.A. Ims and X. Lambin. Spatial population dynamics: analyzing patterns and processes of population synchrony. *Trends in ecology and evolution*, 14:427–431, 2000.

[75] O.N. Bjornsatd and J. Bascompte. Synchrony and second-order spatial correlation in host-parasitoid systems . *Journal of Animal Ecology*, 70:924–933, 2001.

[76] J. Bragard, S. Boccaletti and H. Mancini. Asymmetric coupling effects in the synchronization of spatially extended chaotic systems . *Phys. Rev. Lett.*, 91:064103, 2003.

[77] E. Doedel, R. Paffenroth, A. Champneys, T. Fairgrieve, Yu. Kuznetsov, B. Oldaman, S. Sonstade and X. Wong. *Auto 2000: Continuation and bifurcation software for ordinary differential equations (with Homcont)*. Technical Report, Concordia University, 2002.

[78] P.C. Dauby and L. Lebon. Bénard-Marangoni instability in rigid rectangular containers. *J. Fluid Mech.*, 329:25–64, 1996.

[79] N. Baba, A. Amann, E. Scöll and W. Just. Giant improvement of time-delayed feedback control by spatio-temporal filtering. *Phys. rev. Lett.*, 89:074101, 2002.